

## TOWARDS A GLOBAL EVOLUTIONARY MODEL OF PROTOPLANETARY DISKS

XUE-NING BAI

Institute for Theory and Computation, Harvard-Smithsonian Center for Astrophysics, 60 Garden St., MS-51, Cambridge, MA 02138  
*Draft version March 3, 2016*

## ABSTRACT

A global evolution picture of protoplanetary disks (PPDs) is key to understanding almost every aspect of planet formation, where standard  $\alpha$ -disk models have been constantly employed for its simplicity. In the mean time, disk mass loss has been conventionally attributed to photoevaporation which controls disk dispersal. However, a paradigm shift towards accretion driven by magnetized disk winds has been realized in the recent years, thanks to studies of non-ideal magneto-hydrodynamic effects in PPDs. I present a framework of global PPD evolution aiming to incorporate these advances, highlighting the role of wind-driven accretion and wind mass loss. Disk evolution is found to be largely dominated by wind-driven processes, and viscous spreading is suppressed. The timescale of disk evolution is controlled primarily by the amount of external magnetic flux threading the disks, and how rapidly the disk loses the flux. Rapid disk dispersal can be achieved if the disk is able to hold most of its magnetic flux during the evolution. In addition, because wind launching requires sufficient level of ionization at disk surface (mainly via external far-UV radiation), wind kinematics is also affected by far-UV penetration depth and disk geometry. For typical disk lifetime of a few Myrs, the disk loses approximately the same amount of mass through the wind as through accretion onto the protostar, and most of the wind mass loss proceeds from the outer disk via a slow wind. Fractional wind mass loss increases with increasing disk lifetime. Significant wind mass loss likely substantially enhances the dust to gas mass ratio, and promotes planet formation.

*Subject headings:* accretion, accretion disks — magnetohydrodynamics — methods: numerical — planetary systems: protoplanetary disks

## 1. INTRODUCTION

Global evolution of protoplanetary disks (PPDs) is governed by the processes of angular momentum transport and outflow mass loss. These processes directly control disk structure and evolution, which set the timescales of disk dispersal and hence planet formation (e.g., see Armitage 2011; Turner et al. 2014 and Alexander et al. 2014 for reviews). They also strongly affect the evolution of dust grains, which are building blocks of planets, and feedback to disk thermal and chemical structures (e.g., see Testi et al. 2014 and Henning & Semenov 2013 for reviews). If planets are formed within the disk lifetime, planet-disk interaction leads to planet migration, which is also sensitive to global disk structure and evolution (e.g., see Baruteau et al. 2014 for a review). In brief, a reliable global evolutionary picture of PPD is key to understanding most processes of planet formation.

Most PPD models used in planet formation research are constructed upon the viscous  $\alpha$  disk model (Shakura & Sunyaev 1973), where the underlying assumption is that the disk is turbulent presumably due to the magneto-rotational instability (MRI, Balbus & Hawley 1991). However, the extremely weak level of ionization introduces strong non-ideal magneto-hydrodynamic (MHD) effects that suppress or damp the MRI in most regions in PPDs, while pure hydrodynamic mechanisms appear unable to provide sufficiently level of turbulent viscosity (e.g., Turner et al. 2014). Angular momentum transport in PPDs is thus most likely governed by magnetized disk winds, as demonstrated

in disk simulations that properly taking into account these non-ideal MHD effects (e.g., Bai & Stone 2013b; Bai 2013, 2014, 2015; Lesur et al. 2014; Gressel et al. 2015; Simon et al. 2015). In the mean time, the MRI may operate in the surface layer of the outer disk, owing to strong far-UV (FUV) ionization at disk surface (Perez-Becker & Chiang 2011), which can lead to vigorous turbulence and mediate a certain level of viscous transport of angular momentum (Simon et al. 2013b,a; Bai 2015).

We note that in the conventional studies of MHD winds, wind launching generally requires near equipartition field at the disk midplane (e.g., Ferreira & Pelletier 1995). As a result, the disk surface density must be very low to be consistent the observed disk accretion rates (e.g., Combet & Ferreira 2008, otherwise, accretion rate would become too high), making the disk wind scenario less appealing to account for the mass content of gas and dust in PPDs. On the other hand, in the aforementioned more realistic simulations, winds are launched from several scale heights above midplane, because the midplane region is too weakly ionized for sufficient coupling between the gas and magnetic fields. With much weaker field (magnetic pressure much less than midplane gas pressure) permitted for wind launching, the new scenario simultaneously accounts for the accretion rates and mass budget from observations.

The paradigm shift towards wind-driven PPD evolution calls for a model framework in replacement of  $\alpha$ -disk models. The aforementioned simulations are all local in vertical extent, and hence are unable to provide reliable estimates of wind kinematics. An initial study

by Armitage et al. (2013) took the fitting relations of viscous stress and wind torque from Simon et al. (2013a)'s outer disk simulations and found slow disk evolution followed by rapid dispersal. Disk mass loss was not included in their study. A more reliable disk evolution framework would require better determination of the wind torque and wind mass loss rate, and their dependence on physical parameters.

Recently, Bai et al. (2016) (hereafter B16) proposed a physically motivated, semi-analytical 1D model of PPD disk winds with global treatment of wind kinematics. The model further takes into account thermodynamical effects and unifies the classical (cold) MHD disk wind with photoevaporation. Despite remaining uncertainties explicitly discussed there, it now becomes possible to incorporate the key results into a framework of global wind-driven PPD evolution, and explore in parallel the role played by magnetic fields and thermodynamics. This is the goal of this paper.

We describe our formalism and methodology in Section 2. In Section 3, we discuss the general angular momentum transport and mass loss processes without evolving the disk, and study parameter dependence. Disk evolutionary properties are studied in Section 4. We extend our model to discuss additional effects including level of disk flaring and X-ray heating in Section 5. Implications and limitations of our study are discussed in Section 6. We summarize and conclude in Section 7.

## 2. A SIMPLIFIED MODEL FOR WIND-DRIVEN PPD EVOLUTION

We construct a 1 D disk model on the evolution of the disk surface density  $\Sigma(R)$  as a function of disk cylindrical radius  $R$  in the presence of turbulence, wind torque and mass loss (Section 2.1). In the mean time, we adopt a simple treatment of disk vertical structure to estimate the vertical location  $z_a$  where external far-UV (FUV) radiation can penetrate, and  $z_b$  ( $\geq z_a$ ) where the wind is launched (wind base), based on which we calculate the transport properties (Section 2.2). Hence, our model can be considered as 1+1 D. We discuss calculation procedures and model parameters in Section 2.3.

### 2.1. Disk Evolutionary Equations

We begin by writing down the equations governing the surface density evolution, incorporating the effects of viscosity, wind torque and mass loss. Let  $\dot{M}_{\text{acc}}(R)$  be the net accretion rate at cylindrical radius  $R$ . We adopt the sign convention such that  $\dot{M}_{\text{acc}}$  is positive for net accretion. Let  $\dot{M}_{\text{loss}}(R)$  be the cumulative wind mass loss rate enclosed within radius  $R$ . We will always use its differential form

$$\dot{M}_{\text{loss}}(R) \equiv \int_{R_i}^R \frac{\partial \dot{M}_{\text{loss}}}{\partial R} dR', \quad (1)$$

where  $R_i$  is the radius of the disk inner edge beyond which the wind is launched.

The bulk of PPDs is cold, and unless unrealistically strongly magnetized, rotation is largely Keplerian, with specific angular momentum  $j_K(R) = v_K R = \Omega_K R^2$ , where  $v_K, \Omega_K$  are the Keplerian speed and corresponding angular frequency. Let  $\dot{J}_r(R)$  be the vertically integrated

total radial angular momentum flux. It is given by

$$\dot{J}_r = -\dot{M}_{\text{acc}}(R)j_K(R) + W_r(R), \quad (2)$$

where

$$\begin{aligned} W_r(R) &= 2\pi R^2 \int_{-z_b}^{z_b} dz \left( \overline{\rho \delta v_R \delta v_\phi} - \frac{\overline{B_R B_\phi}}{4\pi} \right) \\ &\equiv 2\pi R^2 \int_{-z_b}^{z_b} dz \alpha(z) \rho c_s^2 \equiv 2\pi R^2 \tilde{\alpha} \Sigma c_s^2 \end{aligned} \quad (3)$$

accounts for angular momentum flux generated from internal stresses, including Reynolds stress, Maxwell stress, and potentially stress from disk self-gravity (not included above) in the case of a massive disk that is gravitationally unstable, with overline representing averaging over the local volume. Here, we follow the  $\alpha$  convention, with  $c_s$  being disk sound speed. Note that  $\alpha$  can be position dependent, and we use  $\tilde{\alpha}$  to represent an effective, (density-weighted) vertically-averaged value.

Let  $\dot{J}_w(R)$  be the total vertical angular momentum flux extracted from the disk (by the MHD wind) enclosed within radius  $R$ . We only use its differential form:

$$\begin{aligned} \frac{\partial \dot{J}_w(R)}{\partial R} &= 2\pi R^2 \left( \overline{\rho v_z v_\phi} - \frac{\overline{B_z B_\phi}}{4\pi} \right) \Big|_{-z_b}^{z_b} \\ &= \frac{\partial \dot{M}_{\text{loss}}}{\partial R} j_K + \frac{\partial W_w(R)}{\partial R} \approx \lambda(R) \frac{\partial \dot{M}_{\text{loss}}}{\partial R} j_K, \end{aligned} \quad (4)$$

where

$$\frac{\partial W_w(R)}{\partial R} = 2\pi R^2 \left( -\frac{\overline{B_z B_\phi}}{4\pi} \right) \Big|_{-z_b}^{z_b} = (\lambda - 1) \frac{\partial \dot{M}_{\text{loss}}}{\partial R} j_K, \quad (5)$$

and  $\lambda$  is called the wind lever arm (dimensionless). For wind launched from radius  $R_0$ , the physical meaning of  $\lambda(R_0)$  is that it is the ratio of specific angular momenta in the wind flow and in the Keplerian disk at  $R = R_0$ , and it is related to wind Alfvén radius  $R_A$  by  $\lambda \equiv (R_A/R_0)^2 > 1$ . The  $\partial W_w/\partial R$  term represents the *excess* angular momentum extracted from the disk, related to the wind torque. In the above, we have dropped the hydrodynamic term in the definition of  $W_w$ , which corresponds to the standard definition of the wind base  $z_b$  (Wardle & Koenigl 1993): at the wind base,  $v_\phi(z_b) = v_K$ .

Disk continuity and angular momentum conservation equations read

$$2\pi R \frac{\partial \Sigma}{\partial t} = \frac{\partial \dot{M}_{\text{acc}}}{\partial R} - \frac{\partial \dot{M}_{\text{loss}}}{\partial R}, \quad (6)$$

$$\frac{\partial}{\partial t} (2\pi R \Sigma j_K) = -\frac{\partial \dot{J}_r}{\partial R} - \frac{\partial \dot{J}_w}{\partial R}. \quad (7)$$

With preparations above, they can be combined to

$$2\pi R \frac{\partial \Sigma}{\partial t} = \frac{\partial}{\partial R} \left[ \frac{dR}{dj_K} \left( \frac{\partial W_r}{\partial R} + \frac{\partial W_w}{\partial R} \right) \right] - \frac{\partial \dot{M}_{\text{loss}}}{\partial R}, \quad (8)$$

where the two terms in the parenthesis represent accretion rate driven by viscosity and wind, respectively, and

the equation can further be rearranged to

$$2\pi R \frac{\partial \Sigma}{\partial t} = \frac{\partial}{\partial R} \left[ \frac{2}{v_K} \frac{\partial}{\partial R} (2\pi R^2 \tilde{\alpha} \Sigma c_s^2) \right] + \frac{\partial}{\partial R} \left[ 2(\lambda - 1) R \left( \frac{\partial \dot{M}_{\text{loss}}}{\partial R} \right) \right] - \frac{\partial \dot{M}_{\text{loss}}}{\partial R}. \quad (9)$$

This is the master equation that we will solve to study global disk evolution.<sup>1</sup> It clearly generalizes the viscous evolution equation to include wind-driven accretion and mass loss terms (the 2nd and 3rd terms on the right hand side). To evaluate these terms, we must determine  $\tilde{\alpha}$ ,  $\lambda$  and  $\partial \dot{M}_{\text{loss}} / \partial R$  at each radius, as we do in the next subsection.

## 2.2. The Model for Disk Structure, Angular Momentum Transport, and Mass Loss

We follow and extend the work of B16 and construct the vertical dimension of our wind model to calculate wind properties, and the basic picture is illustrated in Figure 1.

We assume that the disk follows a two-temperature profile with  $T = T_d$  in the disk interior and  $T = T_a$  at disk surface (atmosphere), and transitions at vertical height  $z = z_a$ . Both layers are treated as vertically isothermal. Disk temperature  $T_d$  is largely determined by stellar irradiation. We use a power-law temperature profile similar to the standard minimum-mass solar nebular (MMSN) model (Weidenschilling 1977; Hayashi 1981) with

$$T_d = 280 \text{ K } R_{\text{AU}}^{-s_T}, \quad (10)$$

where  $R_{\text{AU}}$  is radius measured in AU, and  $s_T$  is the power law index. By default, we take  $s_T = 1/2$ , as in the MMSN model. The corresponding disk isothermal sound speed  $c_{s,d}$  and disk scale height  $H_d$  satisfy  $c_{s,d}/v_K = (H_d/R) \approx 0.034 R_{\text{AU}}^{1/4}$ . With  $H_d/R$  increasing with  $R$ , the disk is flared, as is well known from SED modeling of T Tauri disks (Chiang & Goldreich 1997).

Disk surface (atmosphere) temperature is largely determined strong heating from stellar far-UV (FUV) radiation and X-rays. For simplicity, we assume it is a constant factor higher than disk temperature

$$T_a = f T_d, \quad (11)$$

and hence atmosphere sound speed  $c_{s,a} = \sqrt{f} c_{s,d}$ . In practice, we take  $f = 3 - 8$  in our calculations, consistent with typical results from more detailed thermochemical calculation (e.g., Walsh et al. 2010), as well as observational constraints from the HD 163296 disk (Rosenfeld et al. 2013).

In the mean time, FUV is capable of fully ionizing carbon and sulfur species, leading to an ionization fraction  $\sim 10^{-5-4}$ , and gas and magnetic fields become well coupled in the FUV layer (Perez-Becker & Chiang 2011). We note that X-rays alone generally produces much lower

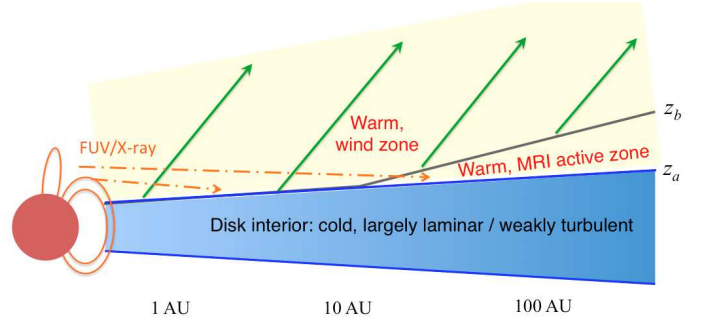


FIG. 1.— Cartoon illustration of our global PPD evolution model. The bulk of the disk is cold (thin), where magnetic fields are poorly coupled to the gas with very weak level of turbulence. The surface layer is much warmer and much better ionized due to strong external far-UV/X-ray heating/ionization, and the gas is well coupled to magnetic fields, enabling MHD wind launching. The cold-warm interface is marked by  $z_a$ , and we use  $z_b$  to denote the wind base where the wind is launched. In general,  $z_b \approx z_a$  unless net vertical magnetic field is not sufficiently strong. In this case, the warm surface layer can become MRI active (achieved at the outer disk), and  $z_b > z_a$ , sandwiching a warm MRI layer. Not reflected in this cartoon picture is that the disk is flared, making FUV radiation easier to penetrate into the outer disk.

level of ionization in the surface layer (e.g., cf. Figure 1 of Bai 2011). Launching of MHD winds requires sufficient coupling between gas and magnetic fields, and hence it mainly relies upon FUV ionization. Let  $\Sigma_{\text{FUV}}$  be the characteristic penetration depth of FUV photons. Its value is uncertain and depends on the FUV luminosity from the protostar, as well as the abundance of very small grains. Here we adopt the calculation results by Perez-Becker & Chiang (2011), quoting

$$\Sigma_{\text{FUV}} = 0.01 - 0.1 \text{ g cm}^{-2}, \quad (12)$$

and treat it as a constant at all radii. The location of the FUV front is determined by tracing radial rays from the central star, until the column density traversed by the rays equals to  $\Sigma_{\text{FUV}}$  (see Section 2.2.4 for details).

By default, we assume that the penetration depth of FUV and X-rays are comparable so that  $z_a$  is determined by  $\Sigma_{\text{FUV}}$ . In other words, we assume the rapid increase of temperature at  $z = z_a$  is accompanied by a transition into ideal MHD regime at disk surface. In reality, X-rays may be able to provide heating into deeper layers. This will be discussed in Section 5.2, where we relax this assumption.

Another important location is the wind base  $z_b$ , from which the wind is launched. The wind model of B16 assumed  $z_b = z_a$  motivated by numerical simulations of the inner disk (Bai & Stone 2013b; Gressel et al. 2015). Towards the outer disk, however, FUV can effectively penetrate deeper into the disk (in terms of  $z_a/H_d$ ) as the disk is flared, and this can make the surface layer subject to the MRI (Perez-Becker & Chiang 2011). A disk wind can also be launched from the surface MRI turbulent layer in the presence of net vertical field (Suzuki & Inutsuka 2009; Fromang et al. 2013; Bai & Stone 2013a; Suzuki & Inutsuka 2014), and local simulations applicable to the outer PPDs found evidence that disk outflow is launched from a higher position than the FUV front (Simon et al. 2013a). We describe a prescription in Section 2.2.4 to approximately determine the location of  $z_b > z_a$  in this case, and treat the layer

<sup>1</sup> Note that the term involving  $\alpha$  is a factor 2/3 of that in a viscous evolution equation. This is because we directly parameterize  $\alpha$  from the  $R\phi$  component of the stress tensor  $T_{R\phi}$  (the terms in the parenthesis in Equation (3)), whereas assuming Navier-Stokes viscosity  $\nu$ ,  $T_{R\phi}$  involves  $d\Omega/dR$  which yields an extra factor of 3/2.



$z_a < z < z_b$  as being MRI active. We apply the B16 model in the wind zone at  $z > z_b$ , from which we estimate the wind mass loss rate and wind torque. Although the B16 model was constructed assuming laminar flows and does not strictly apply to estimate the wind kinematics of outflows launched from a turbulent surface, we assume that it can still provide a reasonable approximation in terms of wind mass loss rate and angular momentum transport.

Below, we first construct the wind model assuming the locations of  $z_a$  and  $z_b$  are known, then we iteratively determine their locations.

### 2.2.1. Choice of the B16 Wind Model Parameters

The B16 wind model is constructed from the wind base  $z_b$ . Being a wind model that takes into account both magnetic and thermal effects, the most important parameters are the net vertical magnetic field strength  $B_z(R)$  threading the disk and wind/atmosphere temperature  $T_a$  (or the atmosphere sound speed  $c_{s,a}$ ). We treat them as our main physical parameters, and they correspond to  $B_{p0}$  and  $c_{s,w}$  defined in the B16 model.

We will discuss our choice of  $B_z(R)$  in Section 2.2.3. Concerning wind temperature  $T_a$ , characterized by the  $f$  factor in (11), we apply an additional constraint such that the ratio of surface sound speed to Keplerian velocity  $c_{s,a}/v_K \leq 0.2$ . The B16 model tends to be less reliable at higher temperature because the slow magnetosonic point is generally located below the wind base, violating the assumptions made there. However, we expect this compromise to have only minor impact in our calculations. As discussed in B16 (see their Figure 12), wind kinematics is not very sensitive to wind temperature, which we also confirm in our global disk calculations in Section 3.2.3.

We fix other parameters considered in B16 at their fiducial values, where it was found that the wind solutions are generally not sensitive to these parameters. In particular, wind properties are not very sensitive to the field inclination angle  $\theta$  because the wind is warm. We thus choose representative field geometry parameters  $\theta = 45^\circ$ . We also choose the field divergence parameter to be  $q = 0.25$ .<sup>2</sup> We refer to Section 2 of B16 for further model details.

### 2.2.2. Vertical Density Profile

At each radius  $R$ , the disk zone at  $z < z_a$  satisfies hydrostatic equilibrium, and gas density profile  $\rho$  within the disk is simply

$$\rho(R, z) = \rho_m(R) \exp \left[ -\frac{z^2}{2H_d(R)^2} \right] \quad (z < z_b) \quad (13)$$

where  $\rho_m$  is midplane gas density. At the location  $z = z_a$ , pressure balance requires a density jump between the disk side and the atmosphere side

$$\rho|_{z=z_a^-} T_d = \rho|_{z=z_a^+} T_a, \quad (14)$$

<sup>2</sup> This parameter characterizes how rapidly field strength approaches the  $B_p \propto R^{-2}$  scaling (see Equation 2 of B16 for definition), and the wind solutions do show relatively strong dependence on  $q$ . We choose the fiducial number  $q = 0.25$  to avoid more extreme cases (i.e., diverging from launching point with  $q = \infty$  and field lines being parallel to large distances).

and we define  $\rho_a \equiv \rho|_{z=z_a^+}$ . While this jump should occur more smoothly in reality where temperature transition is more smooth, the resulting uncertainty can be absorbed into  $\Sigma_{\text{FUV}}$ . Between  $z_a \leq z \leq z_b$ , another hydrostatic equilibrium is maintained as

$$\rho(R, z) = \rho_a(R) \exp \left[ -\frac{z^2 - z_a^2}{2H_a(R)^2} \right] \quad (z_a \leq z \leq z_b), \quad (15)$$

where  $H_a = \sqrt{T_a/T_d} H_d$  is the scale height of the disk atmosphere. Typically, the wind base is located at several disk scale heights above midplane, and regions with  $z < z_b$  encloses most of the disk mass. Thus, midplane density  $\rho_m$  can be determined from surface density  $\Sigma$  once  $z_a$  is known.

For the purpose of locating the wind base (see Section 2.2.4), we also need the density profile in the vicinity of the wind base so as to calculate the column densities for FUV ray tracing. Due to magnetic forces, it can deviate substantially from hydrostatic equilibrium. From Figure 3 of B16, we see that at fixed wind temperature  $c_{s,w} = 0.1v_K$ , the wind density profile is almost independent of wind magnetization up to a substantial distance ( $\sim 2$  times wind launching radius) from the wind base. We have also verified this trend with other choices of wind temperature. For wind launched from radius  $R_0$ , we find a reasonable fitting formula for gas density profile along the wind streamline

$$\rho(R) \approx \rho_b(R_0) \exp \left[ -\left( \frac{c_{s,a}}{v_K} \right)^{-0.6} \sqrt{\frac{R}{R_0} - 1} \right], \quad (16)$$

where  $\rho_b$  is gas density at the wind base from (15), and  $R$  is cylindrical radius along the wind streamline. This formula is accurate to within order unity (most cases within  $\sim 20\%$ ) up to  $R = 2R_0$  for wind temperature range  $c_{s,a}/v_K = 0.05 - 0.3$ . Because this density profile is solely used for finding the wind base location, we may convert it into a vertical density profile at radius  $R_0$  and  $z > z_b$  for convenience

$$\rho(R_0, z) = \rho_b(R_0) \exp \left[ -\left( \frac{c_{s,a}}{v_K} \right)^{-0.6} \sqrt{\frac{z - z_b}{R_0}} \right], \quad (17)$$

because FUV photons penetrate through approximately the same column density in these two cases to reach the next wind streamline.

### 2.2.3. Magnetic Flux Distribution and Evolution

Net vertical field strength threading the disk  $B_z$  is associated with the poloidal field at the wind base  $B_{p0}$  by  $B_z \approx B_{p0} \cos \theta$ , where we fix inclination angle  $\theta = 45^\circ$ . It is then reflected in the wind base Alfvén speed  $v_{A0} = B_{p0}/\sqrt{4\pi\rho_b}$ , a crucial parameter in the B16 wind model.

The radial profile of  $B_z(R)$ , and its time evolution, however, are largely unconstrained. Attempts to study magnetic flux transport so far have not considered effects other than viscosity and Ohmic resistivity, nor on the effect of wind-driven accretion (Lubow et al. 1994; Okuzumi et al. 2014; Takeuchi & Okuzumi 2014; Guilet & Ogilvie 2014).<sup>3</sup> We here simply consider a phenomenological approach, as adopted in Armitage et al.

<sup>3</sup> Guilet & Ogilvie (2012) considered the effect of disk outflow

(2013), and assume that magnetic flux is distributed in such a way that midplane plasma  $\beta$  of the net vertical field,

$$\beta_0(z=0) = \frac{8\pi P_{\text{mid}}}{B_z(R)^2} \quad (18)$$

is constant, where  $P_{\text{mid}} = \rho_m c_{s,d}^2$  is midplane gas pressure.

We further consider two scenarios on the evolution of total magnetic flux  $\Phi_B = 2\pi \int_{R_i}^{R_o} B_z(R) R dR$ . In the first scenario, we assume  $\Phi_B$  is conserved during disk evolution. Therefore, as accretion proceeds, disk becomes more strongly magnetized. In the second scenario, we assume that the disk loses magnetic flux in a way such that  $\Phi_B$  is proportional to total disk mass  $M_d = 2\pi \int_{R_i}^{R_o} \Sigma(R) R dR$ . This treatment avoids significant accumulation of magnetic flux and results in slower evolution.

It is conceivable that magnetic flux evolution can have major impact on global disk structure and evolution, and our phenomenological treatment bares significant uncertainties. For instance, it has been found that the MRI can concentrate vertical magnetic flux into ring-like structures (Steinacker & Papaloizou 2002; Bai & Stone 2014), accompanied by radial pressure variations known as zonal flows (Johansen et al. 2009a). HL Tau like structures (ALMA Partnership 2015) may simply be a manifestation of such zonal flows. Before a more reliable theory of magnetic flux transport is available, we mainly discuss the general features of wind-driven disk evolution without focusing on the details in the evolution of surface density profiles, and explore the general role played by macroscopic parameters such as total magnetic flux and FUV penetration depth so as to better understand the interplay between magnetic and thermal effects on disk evolution and dispersal.

#### 2.2.4. Determining $z_a$ and $z_b$

Once the vertical density profile is obtained from our 1+1D calculation, we trace radial rays from the origin (stellar location) with different inclination angles  $\theta$  (w.r.t. disk midplane) to calculate the column density  $\Sigma_c(R, z = R \tan \theta)$  traversed by these rays. The location of the FUV ionization front  $z_a$  is determined by  $\Sigma_c(R, z_a) = \Sigma_{\text{FUV}}$ . While this simple ray-tracing procedure ignores important effects of scattering and self-shielding (Bethell & Bergin 2011), particularly on the Lyman- $\alpha$  photons, which dominates FUV luminosities (Herczeg et al. 2004), we again expect the uncertainties can be absorbed into the value of  $\Sigma_{\text{FUV}}$ , as a first approximation.

Additionally, knowing the net vertical field strength  $B_z$ , we can estimate the plasma  $\beta$  of the net vertical field at  $z = z_a$ :  $\beta_0(z_a) = 8\pi \rho_a c_{s,a}^2 / B_z^2$ . We note that in the ideal MHD regime, the most unstable MRI wavelength is given by (e.g., Hawley et al. 1995)

$$\frac{\lambda_m}{H_a} \approx 9.18 \beta_0^{-1/2}. \quad (19)$$

in their local model though it was treated in the limit  $B_\phi \ll B_z$  at disk surface. We expect PPD wind to lie in the opposite limit.

Due to the rapid density drop with height, we expect the MRI to be able to effectively operate when  $\lambda_m \lesssim H_a$ . In practice, we assume that the disk surface becomes MRI turbulent when  $\beta_0(z_a) > 50$ . Otherwise, we directly set  $z_b = z_a$ .

If  $\beta_0(z_a) > 50$ , we would expect the wind to be launched from higher location from the MRI turbulent layer. We further follow the density profile using (15) and determine the wind base location  $z_b$  by setting  $\beta_0(z_b) = 50$ . This treatment is by no means rigorous, yet without better knowledge of the wind launching process from turbulent disk surfaces and its global kinematics, we expect it to be a reasonable first approximation. Local simulations of Simon et al. (2013a) lend support to this treatment in that following a generalized (yet unproved) procedure to determine  $z_b$ , they found that  $z_b$  is located above the FUV ionization front, and becomes higher when net vertical field is weaker. We also note that in their simulations where the disk becomes largely laminar (AD30AU1e3 and AD30AU1e4L),  $\beta_0$  at the wind base is about 35 and 60, which are in rough agreement with our choice of threshold  $\beta_0 = 50$ .

The procedures above to determine  $z_a$  and  $z_b$  can be iterated with the vertical density profile calculations described in Section 2.2.2. Note that iteration only needs to be done at the beginning to establish the initial condition, where convergence can be achieved to within 0.1% typically within 3-4 iterations. The subsequent disk evolution is sufficiently slow that no iteration is necessary.

#### 2.2.5. Effective Viscosity

Pure hydrodynamic instabilities, such as the vertical shear instability (Nelson et al. 2013; Stoll & Kley 2014), convective overinstability and baroclinic vortex amplification (Klahr & Hubbard 2014; Lyra 2014; Raettig et al. 2013), and the zombie vortex instability (Marcus et al. 2014), may operate in certain regions of PPDs largely depending on disk thermodynamics. In general, these instabilities are found to produce very limited viscous transport with  $\alpha < 10^{-3}$ . In this work, we adopt  $\alpha = \alpha_0 = 2 \times 10^{-4}$  at locations  $z < z_a$  to represent residual “viscosity” from such hydrodynamic instabilities. As we shall see, because of the dominant role played by disk winds, the exact value of  $\alpha_0$  adopted here is unimportant.

If an MRI active zone is present, we set  $\alpha = \alpha_1 = 0.2$  in this region ( $z_a < z < z_b$ ). We choose a relatively large  $\alpha$  because the net vertical field at this surface layer is effectively strong (with  $\beta_0$  of the order 100), and it is well known from MRI simulations (e.g., Hawley et al. 1995) that the resulting  $\alpha$  is larger than zero net flux case and is of the order 0.1 or higher.

Additionally, while transport by the MRI is suppressed or strongly damped by non-ideal MHD effects at  $z < z_a$ , there is still Maxwell stress resulting from either weak MRI turbulence or large-scale fields in the outer disk, and its strength increases with net vertical magnetic flux. Incorporating all these considerations, we adopt the following form of  $\alpha$  in the disk zone at  $z < z_a$ :

$$\alpha_d = \text{Min}[\text{Max}(5.0\beta_0^{-1}, \alpha_0), \alpha_1], \quad (20)$$

where the dependence on midplane  $\beta_0$  approximately reflects the stress level found from local simulations of lay-

ered accretion in the presence of net vertical field (e.g., Okuzumi & Hirose 2011; Simon et al. 2013a; Bai 2015).

<sup>4</sup> This way, the  $\alpha_d$  value ranges from  $\alpha_0$  for the weak field case to  $\alpha_1$  for the strong field case which joins the  $\alpha$  value in the surface MRI active zone. Although this prescription is motivated by the outer PPD gas dynamics, we simply apply it to the entire disk, allowing  $\alpha$  to increase with net  $B_z$ . Towards the inner disk where the Hall effect is important, this treatment also roughly reflects the fact that the large-scale stress (magnetic braking) resulting from the Hall-shear instability increases with net vertical flux (Lesur et al. 2014; Bai 2014).<sup>5</sup> We further comment that the overall disk evolution is insensitive to the exact prescription of  $\alpha$  values because, as we will see, disk evolution is largely wind-driven.

We apply the  $\alpha$  values in the disk and surface regions discussed above to Equation (3), from which an effective value,  $\tilde{\alpha}$ , can be determined. Note that we quote the  $\tilde{\alpha}$  value based on sound speed in the disk interior  $c_{s,d}$ .

### 2.2.6. Wind Mass Loss Rate and Lever Arm

Knowing the poloidal Alfvén speed and sound speed  $v_{A0}$  and  $c_{s,a}$  at the wind base, we fit the numerical results presented in B16 to evaluate  $\lambda$  and  $\partial\dot{M}_{\text{loss}}/\partial R$  as needed to evolve the master equation (9).

The wind mass loss rate is characterized by the dimensionless mass loading parameter  $\mu$  given by (see Equation 21 of B16)

$$\frac{d\dot{M}_{\text{loss}}}{dR} \approx \mu \frac{2\pi}{\Omega_K} \rho_b v_{A0}^2 = \frac{\mu}{2\Omega_K} B_{p0}^2. \quad (21)$$

The wind is considered to be heavily loaded when  $\mu \gtrsim 1$ . Figure 5 of B16 shows the dependence of  $\mu$  on  $v_{A0}$  for three different wind temperatures, which we find can be well fitted by

$$\mu = \mu_0 \left( \frac{v_{A0}}{v_K} \right)^{-1.48 + 0.17 \log_{10}(c_{s,a}/v_K) - 0.1 \log_{10}(v_{A0}/v_K)}, \quad (22)$$

where  $\mu_0 = 0.5(c_{s,a}/v_K) - 0.015$ . We have also examined additional wind solutions and confirm that this fitting formula is accurate as long as  $c_{s,a}/v_K \gtrsim 0.033$  (note that it becomes unphysical if  $c_{s,a}/v_K \leq 0.03$ ). For all models considered in this work, the disk surface is sufficiently warm and satisfies this condition.

The magnetic lever arm  $\lambda$  is defined as  $\lambda = (R_A/R_0)^2$ , where  $R_0$  is the wind launching radius and  $R_A$  is the Alfvén radius. As shown in Figure 7 of B16,  $R_A/R_0$  follows a well defined relation with  $\mu$ . The relation is independent of wind temperature when the wind is lightly loaded ( $\mu \ll 1$ ), and is largely parallel to the corresponding relation in the Weber & Davis (1967) wind. With these considerations, we obtain a reasonable fitting rela-

<sup>4</sup> Dependence of  $\alpha$  on  $\beta_0$  is shallower in fully MRI turbulent disks (Sorathia et al. 2010; Gressel & Pessah 2015).

<sup>5</sup> With caveats that the stress level strongly depends on grain abundance (Xu & Bai 2016), and it only applies when the background vertical field is aligned with disk rotation. Nevertheless, in our case wind is always the dominant driving mechanism of angular momentum transport in the inner disk, and the details of the viscosity prescription does not affect the overall disk evolution.

tion

$$\frac{R_A}{R_0} \approx \frac{\sqrt{1.5[1 + (0.2\mu)^{-2/3}]}}{[1 + (0.2\mu)^{1/4}(c_{s,a}/v_K)^2]^2} \quad (23)$$

We find this fitting relation is accurate for  $\mu$  up to 100 for the range of  $c_{s,a}/v_K$  considered in this work ( $\leq 0.2$ ). Note that this fitting relation becomes invalid and would predict  $R_A/R_0 < 1$  for very large  $\mu$  and when the wind is warm. In reality, the wind would transition into a pure thermally driven towards higher temperature, and no longer extracts disk angular momentum. Note that the results presented in B16 all have  $\mu < 100$ , partly because a wind that is too heavily loaded generally violates the assumptions made there (e.g., the slow magnetosonic point is located below the wind base). In practice, because we have imposed the condition  $\beta_0 \leq 50$  at the wind base (relatively strong field), we never encounter a situation with  $\mu > 100$ .

### 2.3. Calculation Procedures and Model Parameters

As a fiducial example and initial condition for our calculations, we consider a disk model with a power-law radial profile and an exponential cutoff motivated from sub-millimeter observations (Andrews et al. 2009, 2010)

$$\Sigma_0(R) = 500 \text{ g cm}^{-2} R_{\text{AU}}^{-1} \cdot \exp(-R/R_d), \quad (24)$$

where  $R_{\text{AU}}$  is radius measured in AU. We choose the cutoff radius to be  $R_d = 100$  AU throughout this work. The total disk mass is about  $0.035 M_\odot$ .

Our calculations are carried out on a logarithmic grid with inner boundary at  $R_i = 0.1$  AU, and outer boundary at  $R_o = 1000$  AU using 200 grid points. Although the disk-magnetosphere boundary likely lies further in, we choose  $R_i = 0.1$  AU because the innermost disk region ( $\lesssim 0.1 - 0.3$  AU) is sufficiently hot for thermal ionization of Alkali species and is expected to be fully turbulent due to the MRI (e.g., Desch & Turner 2015). The dynamics in this region is complex and is very sensitive to disk thermodynamics (e.g., Faure et al. 2014; Hirose 2015), yet a comprehensive picture has not been established (especially with the addition of MHD disk winds). We do not attempt to model the dynamics of this region, but we also point out that this region contains only a very small fraction of total disk mass and should not affect the bulk of disk evolution.

The viscous term in Equation (9) is integrated with standard zero torque boundary conditions. The wind-driven accretion (advection) term is integrated using the standard upwind method. We set  $\Sigma_{\text{min}} = 10^{-4} \text{ g cm}^{-2}$  as a floor of surface density.

Our model mainly consists of three sets of parameters.

First, magnetic flux distribution and evolution. We consider three different values initial magnetic field strength, corresponding to plasma  $\beta$  of the net vertical field at midplane  $\beta_0(z=0) = 10^3, 10^4, 10^5$  and  $10^6$ , with  $\beta_0 = 10^5$  as fiducial value. In each case, we evolve the magnetic flux either assuming flux conservation  $\Phi_B = \text{const}$ , or assuming  $\Phi_B \propto \dot{M}_d$ .

Second, FUV penetration depth. We consider  $\Sigma_{\text{FUV}} = 0.01 \text{ g cm}^{-1}$  and  $0.1 \text{ g cm}^{-1}$ , taking the former as fiducial.

Third, disk atmosphere temperature. We consider two values of  $f = 3$  or  $f = 8$ , with the former as fiducial (see Equation (11)).



We will discuss in Section 5 further extensions of our model, discussing the effect of X-ray heating and the level of disk flaring.

### 3. TRANSPORT PROPERTIES IN A STATIC DISK

We begin by discussing the general features without evolving the disk. We draw the disk surface density profile from (24) and follow the procedures outlined above to calculate the main diagnostic quantities related to disk angular momentum transport and mass loss.

#### 3.1. The Fiducial Model

We first discuss the results from our fiducial set of physical parameters with  $\beta_0 = 10^5$ ,  $\Sigma_{\text{FUV}} = 0.01 \text{ g cm}^{-2}$ ,  $T_a = 3T_d$  and  $s_T = 0.5$ , shown in Figure 2. We focus our discussion on the solid lines in the Figure, and in Section 3.1.3 we discuss the effect of wind shielding by comparing with the dashed lines in the Figure.

##### 3.1.1. Disk Structure

The middle left panel shows the location of the FUV ionization front  $z_a$  and wind base  $z_b$ . We can see that up to  $R \sim 50 \text{ AU}$ , the two locations coincide with each other, meaning that the disk is largely laminar up to this radius, with wind being the dominant mechanism for angular momentum transport. The value of  $z_a/R$  increases with increasing  $R$ , meaning that the FUV ionization front traces a flared geometry. On the other hand, because the disk itself is flared, we see from the inset that when normalized to disk scale height, the value of  $z_a/H_d$  decreases with increasing  $R$ . This means that the FUV radiation effectively penetrates deeper (geometrically) towards the outer disk. The value of  $z_a/H_d$  is  $\lesssim 5$  at 1 AU, and decreases to  $\sim 3.5$  at  $\sim 100 \text{ AU}$ . These numbers are similar to local disk simulations where the FUV penetration depth is measured in the vertical domain (Bai & Stone 2013b; Simon et al. 2013a).

Deeper penetration of FUVs towards the outer disk allows the MRI to operate at  $R \sim 50 \text{ AU}$  and beyond in our fiducial model. Correspondingly, the wind base location  $z_b$  no longer coincides with  $z_a$ , and is located higher in the atmosphere. With  $z_a/H_d$  decreasing with  $R$ , the extent of the MRI zone increases towards larger  $R$ , and hence the value of  $\tilde{\alpha}$  increases towards the outer disk and beyond. Nevertheless, because only a very small fraction of mass resides in the MRI active zone, the averaged value  $\tilde{\alpha}$  remains relatively small ( $\lesssim 10^{-3}$ ).

##### 3.1.2. Accretion and Mass Loss

We find that in the inner disk, the wind Alfvén radius (or lever arm) decreases with increasing  $R$ . This is a consequence of  $z_b/H_d$  getting smaller, and hence when assuming constant midplane  $\beta_0$ , the wind base is less strongly magnetized (larger plasma  $\beta$ , or smaller  $v_{A0}/c_s$ , at the wind base). As a result, the wind becomes less efficient in transporting angular momentum towards larger  $R$ , and the disk has to lose more mass to maintain its accretion rate (i.e., higher mass loading). When the MRI zone is present, because we have set fixed  $\beta_0 = 50$  at the wind base location, the Alfvén radius and mass loading parameter become approximately constants (as found in B16).

The middle right panel of Figure 2 shows the radial profiles of wind-driven accretion rate, viscous accretion rate, and wind mass loss rate per logarithmic radii. We see that clearly, almost the entire disk relies on disk wind to transport angular momentum. The only exception is near the disk outer edge, where disk surface density exponentially falls off and viscous transport picks up. Because of the dominant role played by the wind, viscous disk spread is largely suppressed, except for regions well beyond the characteristic disk size of  $R_d = 100 \text{ AU}$ .

Although we have made an artificial assumption that midplane  $\beta_0$  is constant throughout the disk, the overall wind-driven accretion rate is approximately constant over an extended range of disk radii, indicating that the system shall approximately maintain a steady state. This is related to the our initial disk surface density that we have chosen, where the midplane pressure  $P_{\text{mid}} \propto R^{-11/4}$ . Assuming that the wind-driven accretion rate depends quadratically on the field strength (Wardle 2007; Bai & Goodman 2009), a constant accretion rate would require  $B_z^2 \propto R^{-5/2}$ , whose power law index is very close to  $11/4$ .

The mass loss profile is best quantified by the mass loss rate per logarithmic radii  $d\dot{M}_{\text{loss}}/d\ln R$ , which is related to wind-driven accretion rate by (see B16)

$$\frac{d\dot{M}_{\text{loss}}(R)/d\ln R}{\dot{M}_{\text{acc,w}}(R)} = \frac{1}{2(\lambda - 1)}. \quad (25)$$

As the lever arm  $\lambda \equiv [R_A(R)/R]^2$  decreases towards large  $R$ , we see that wind mass loss rate rapidly increases with  $R$ . The mass loss rate per logarithmic radii is nearly two orders of magnitude below the accretion rate at the innermost radius, while it can become a significant fraction of the accretion rate at tens of AU. Thus, we expect that most of the mass loss in PPDs occurs through the outer disk via very slow winds, in contrast with observations which typically can only trace winds launched from the inner disk (see Section 6.2 for further discussion).

We also note that magnetic field geometry from typical disk wind simulations (e.g., Zanni et al. 2007; Stepanovs & Fendt 2014) has larger inclination angle with respect to the disk at small disk radius ( $\theta > 45^\circ$ ), while  $\theta$  becomes smaller towards the outer disk radii. If we were to relax our assumption of constant field inclination  $\theta = 45^\circ$ , this would make  $\lambda$  larger in the inner disk and smaller in the outer disk (though not by much in a warm wind, as discussed in B16), and hence strengthen our conclusion that mass loss is most significant in the outer disk.

Both wind-driven accretion rate and wind mass loss rate drops when an MRI zone is present. This is can be qualitatively understood from the middle panel of Figure 12 in B16. With the wind launched from higher location hence lower density, both accretion and mass loss rates decreases, and the latter decreases faster. It is this reduction of wind transport that leaves rooms for viscous effect to take over in the outermost region of the disk.

Readers may note a bump at small  $R$  in wind-driven accretion and mass loss rates in Figure 2. This is due to the inability to properly compute FUV penetration near the inner boundaries, but it is only a minor effect and should not affect the overall calculations.

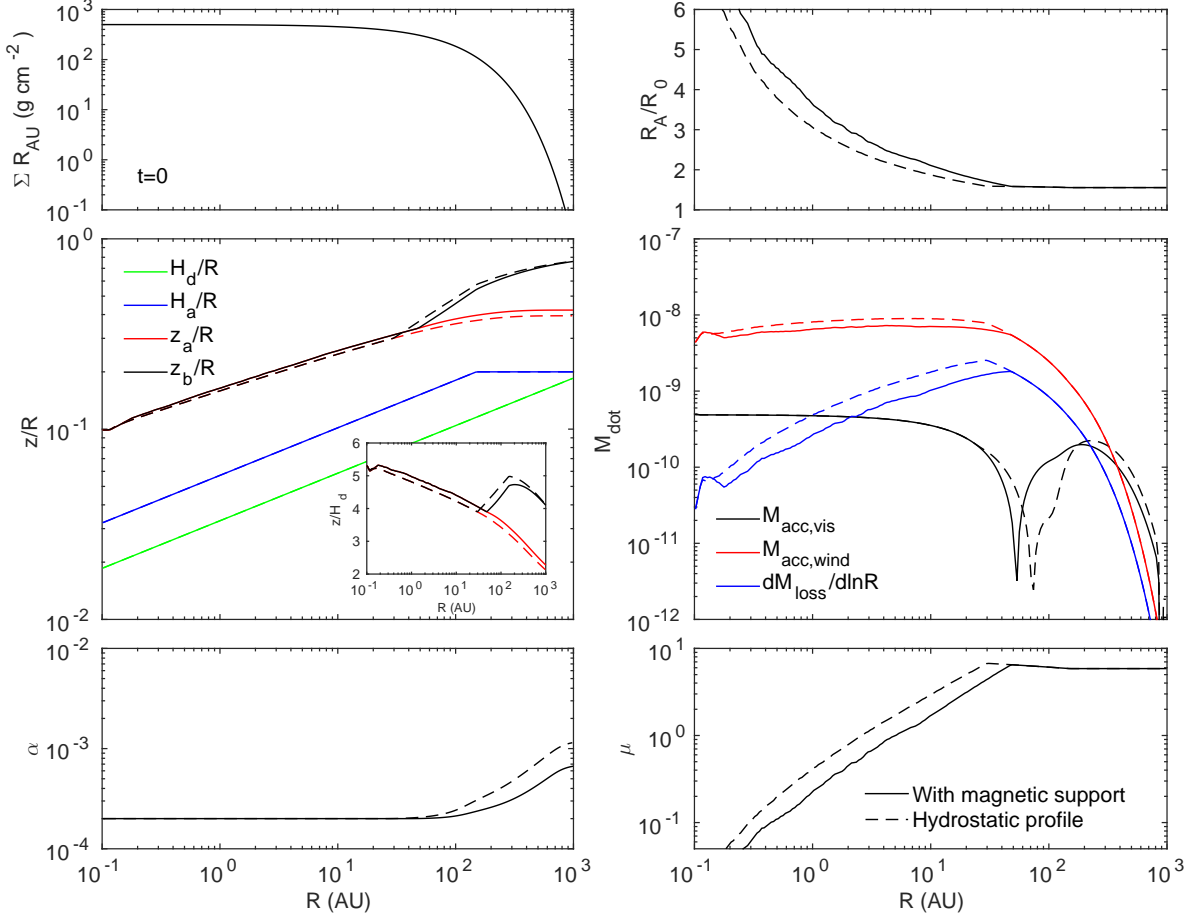


FIG. 2.— Radial profiles of general diagnostics from our fiducial wind model ( $\beta_0 = 10^5$ ,  $\Sigma_{\text{FUV}} = 0.01 \text{ g cm}^{-2}$ , and  $T_a = 3T_d$ ) at the beginning of evolution ( $t = 0$ ) from our fiducial disk model (24). *Top left*: surface density profile (multiplied by  $R/\text{AU}$ ). *Middle left*: location of the wind base  $z_b$  (black), FUV ionization front  $z_a$  (red), together with disk thickness  $H_d$  (green), and disk atmosphere scale height  $H_a$  (blue). They are normalized to  $R$  in the main plot (note we enforce  $H_a/R \leq 0.2$ ), and we further plot  $z_a/H_d$  and  $z_b/H_d$  in the inset. *Bottom left*: effective viscosity  $\alpha$ . Note that we have chosen  $\alpha_0 = 2 \times 10^{-4}$  as a quiescent value throughout the disk. Larger  $\alpha$  values are due to the onset of the MRI. *Top right*: ratio of wind Alfvén radius to wind launching radius. *Middle right*: wind-driven accretion rate (red), viscous-driven accretion rate (black), and wind mass loss rate per logarithmic radii (blue). Note viscous accretion rate changes sign at around  $R \sim 140 \text{ AU}$ . *Bottom right*: mass loading parameter of the disk wind. Solid lines correspond to our fiducial calculation results. For comparison, we further show in dashed lines in all panels the results where we assume hydrostatic density profile (15) extends all the way in the disk atmosphere  $z > z_a$ , instead of using the enhanced density profile (17) beyond the wind base  $z > z_b$  (which incorporates magnetic support).

### 3.1.3. Shielding of FUV by the Wind

Our calculations have incorporated the fact that a disk wind enhances gas density in the disk atmosphere compared with the hydrostatic case, using the approximate fitting formula (17). The enhanced density adds to the column density that FUV radiation has to penetrate, thus providing a certain level of shielding. This shielding effect has been discussed in the context of survival of molecules through various stages of disk evolution (Panoglou et al. 2012). Bans & Königl (2012) further pointed out that strong disk outflow launched from the innermost region of PPDs may suppress the wind launching process at larger radii by shielding FUV/X-ray photons.

To assess the significance of this shielding effect, we also perform a calculation that simply uses the hydrostatic density profile (15) at  $z > z_a$ , and the results are shown in dashed lines in Figure 2.

We see that indeed, using hydrostatic density profile

makes FUV radiation penetrate deeper, giving smaller  $z_a$  at all disk radii. Although the absolute difference in  $z_a$  values is small, it can be more clearly seen in the inset of the middle left panel. Because density drops very rapidly with height in a Gaussian density profile, a small difference in  $z_a$  translates to much larger difference in the density  $\rho_a$  there.

Without shielding, we see that the wind mass loss rate becomes larger by a factor of nearly two. This is because launching the wind from higher density means that the wind is effectively less magnetized, and hence become more heavily loaded (see again from the middle panel of Figure 12 in B16). Thus, the presence of the wind itself helps prevent more severe wind mass loss from the disk (at a modest level). We also note that the wind launched from the thermally ionized, fully turbulent innermost disk, can also contribute to this shielding effect, which is not included in our calculations (see, e.g., Bans & Königl 2012).



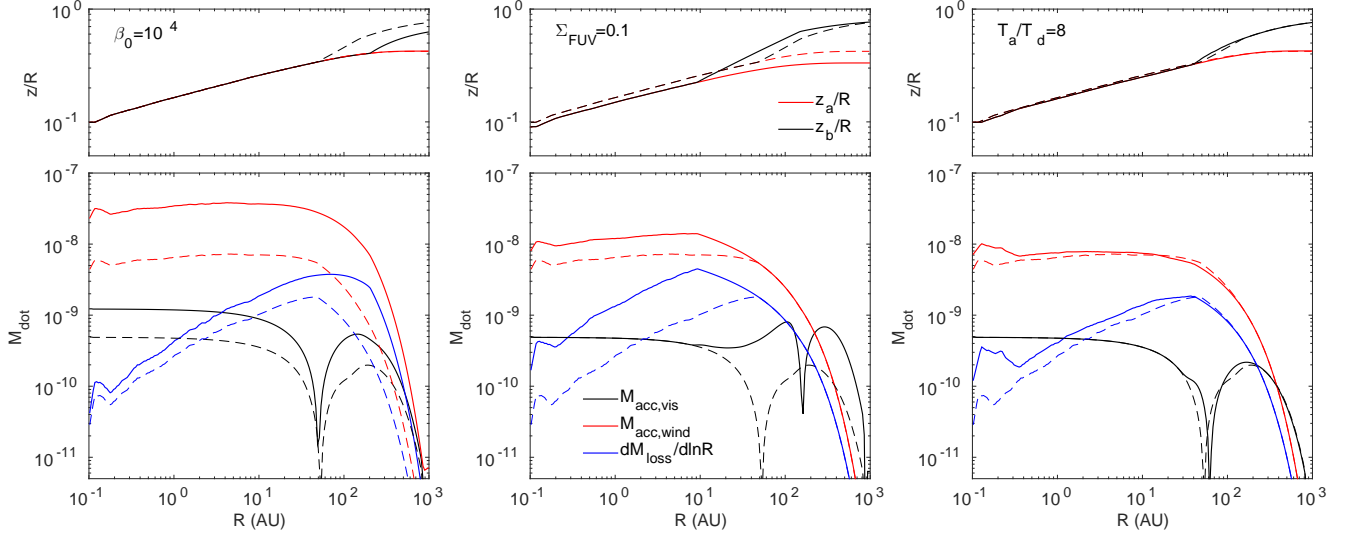


FIG. 3.— Radial profiles of main diagnostics for different physical parameters. For comparison, we show results from the fiducial model in dashed lines (from Figure 2), and we vary only one parameter relative to fiducial in each column and show results in solid lines. Left: enhanced net vertical magnetic flux with  $\beta_0 = 10^4$ ; middle: deeper FUV penetration depth  $\Sigma_{\text{FUV}} = 0.1 \text{ g cm}^{-2}$ ; right: higher disk atmosphere temperature  $T_a = 8T_d$ . Top panels show the location of FUV front  $z_a$  and wind base  $z_b$ , and bottom panels show the radial profiles of wind-driven accretion rate, and viscously-driven accretion rate, and wind mass loss rate.

In addition, we also see that without shielding, the MRI active zone in the outer disk becomes both radially broader and vertically thicker. At each radius, a higher fraction of disk mass is located in the MRI active zone, resulting in a larger  $\tilde{\alpha}$ .

### 3.2. Parameter Dependence

We discuss in this subsection the role played by individual physical parameters, including total magnetic flux (parameterized by midplane  $\beta_0$ ), FUV penetration depth ( $\Sigma_{\text{FUV}}$ ), and atmosphere temperature (characterized by  $T_a/T_d$ ). We vary one parameter at a time. The results are shown in Figures 3 and 4. Note that Figure 4 is exactly analogous to Figure 12 of B16, but applied to a full disk model. In this Figure, we quote accretion rate measured at 1 AU (as discussed earlier, accretion rate profile is largely flat given our magnetic flux prescription). For mass loss, we quote the enclosed mass loss rate (1) within radius of 1 AU, 10 AU and infinity, respectively, to exemplify the mass loss profile.

#### 3.2.1. Role of Vertical Field Strength

The left panels of Figure 3 show the effect of enhanced net vertical magnetic flux, where we choose  $\beta_0 = 10^4$  at midplane. Because density structure in the vicinity of the wind base does not change with magnetization (see Section 2.2.2), the location of  $z_a$  remain largely unchanged. Due to stronger magnetization, the outer disk is less prone to the MRI and the MRI active zone shrinks. While the  $\alpha$  value is larger in the disk interior at all radii to reflect potentially enhanced viscous transport (Section 2.2.5), and yields higher viscous-driven accretion rate, wind plays a more dominant role in global transport: even in the disk outer edge, wind-driven accretion rate overwhelms viscous accretion rate, and hence viscous spread is suppressed.

Stronger vertical fields leads to much enhanced wind-driven accretion rate, but only a modest increase in wind

mass loss rate. This effect is better reflected in the left panel of Figure 4, and has also been extensively discussed in B16. For our fiducial parameters (midplane  $\beta_0 = 10^5$ ), the mass loss rate integrated over the entire disk is about the same as the mass accretion rate. The ratio drops to  $\sim 38\%$  and  $14\%$  for midplane  $\beta_0 = 10^4$  and  $10^3$  respectively. Thus, level of disk magnetization largely controls the fractional mass loss rate over accretion rate.

In addition, we see that mass loss from within 1 AU represents only a very small fraction of total mass loss rate, about 3 – 6%. This fraction increases to about 20 – 30% for mass loss enclosed with  $\sim 10$  AU. Thus, we reinforce the conclusion that most of the mass loss is achieved at the outer disk, which is probably not easily observable.

#### 3.2.2. Role of FUV Penetration Depth

The middle panels of Figure 3 shows the effect of enhanced FUV penetration depth  $\Sigma_{\text{FUV}} = 0.1 \text{ g cm}^{-2}$ . Deeper penetration clearly lowers the location of  $z_a$ . In the inner disk (before the MRI active zone appears), the wind base density and pressure becomes higher, making the wind less strongly magnetized. As discussed in B16, this leads to the development of stronger toroidal field, which drives both higher wind-driven accretion rate, and higher wind mass loss rate. With a reduction of the Alfvén radius, the mass loss rate increases more rapidly. This trend is more clearly seen in the middle panel of Figure 4, and is analogous to the middle panel of Figure 12 in B16. This is a manifestation of what we termed “magneto-photoevaporation” in local wind study of B16 to a global disk model.

In the mean time, deeper FUV penetration enlarges the MRI active zone both radially and vertically, leading to enhanced viscous angular momentum transport. From Figure 3, we see that viscous transport starts to dominate over the wind at a smaller radius than in our fiducial case. Nevertheless, this radius is still larger than our model disk size of  $R_d = 100$  AU, and hence wind transport still

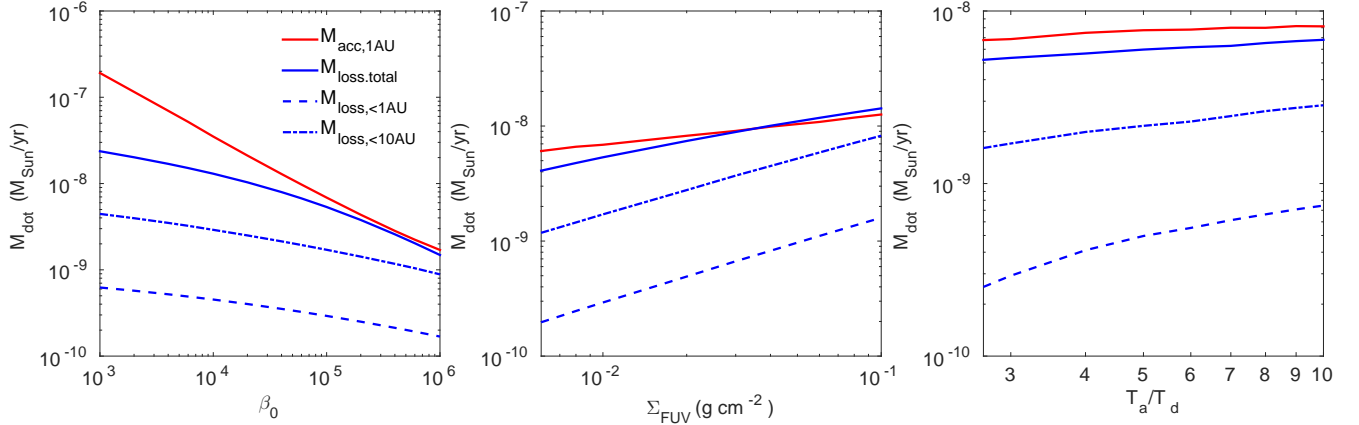


FIG. 4.— Accretion rate at 1 AU (red), cumulative mass loss rate up to 1 AU (blue dashed), 10 AU (blue dash-dotted) and the entire disk (blue solid) as a function of physical parameters. *Left*: dependence on net vertical field strength, parameterized by midplane plasma  $\beta_0$ . *Middle*: dependence on the FUV penetration depth  $\Sigma_{\text{FUV}}$ . *Right*: dependence on the ratio of disk atmosphere temperature  $T_a$  to disk interior temperature  $T_d$ . All calculations are based on our fiducial disk model (24).

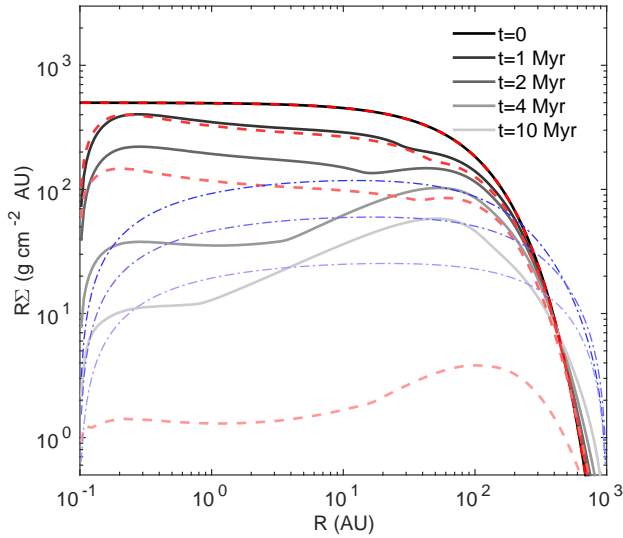


FIG. 5.— Time evolution of disk surface density (given by  $R\Sigma$ ) using our fiducial model parameters. Lines with different transparencies represent different times, as indicated by the legend. Black solid lines correspond to the case where total magnetic flux  $\Phi_B$  is set to be proportional to disk mass  $M_d$ , while red dashed lines represent the case where  $\Phi_B$  is conserved. For comparison, we also show in blue thin dash-dotted lines results from a pure viscous evolution calculations assuming constant  $\alpha = 0.01$  at  $t=1.0, 2.0$  and  $4.0$  Myrs.

dominates the bulk of disk evolution.

We also note that our calculation have ignored external FUV irradiation, which likely dominates over FUV from the star at a few tens to  $\sim 100$  AU scale (Adams et al. 2004), depending on the intensity of the external radiation field and stellar FUV luminosity. Such external irradiation, if sufficiently strong, likely allows FUV to penetrate deeper into the outer disk because they are not shielded by the inner disk. Correspondingly, we would expect the wind to become less effective in the outer disk, where viscous transport likely play a more significant role.

### 3.2.3. Role of Atmosphere Temperature

Disk atmosphere temperature mainly affects wind properties in two ways. First, it directly affects wind properties via thermodynamics, as studied in detail in B16. Second, it modifies the surface density structure. In our two-temperature disk model, a hotter disk surface first leads to a smaller density right above the FUV front due to pressure equilibrium at  $z = z_a$ . On the other hand,  $\rho$  decreases with  $z$  much more slowly at  $z > z_a$ . These two effects turn out to approximately cancel and only weakly affect the geometric depth of FUV penetration, as seen from the right panel of Figure 3.

Assuming the atmosphere temperature does not affect the wind base location, B16 found that the overall wind-driven accretion rate and wind mass loss rate are relatively insensitive to variations in wind temperature. Incorporating the changes in surface density structure, our global calculations show that the same conclusion holds. Further in Figure 4, we see that both mass accretion rate and total mass loss rate are very insensitive to  $T_a/T_d$ .

## 4. GLOBAL DISK EVOLUTION

In this section, we explore the long-term disk evolution based on prescriptions described in Section 2.2. We here mainly focus on the global mass budget, in terms of evolution timescale, fractional mass loss through accretion and wind, etc., to minimize uncertainties associated with the magnetic flux distribution and evolution.

### 4.1. The Fiducial Model

In Figures 5 and 6, we show the time evolution of disk surface density, and the associated disk mass ( $M_d$ ), accretion rate and mass loss rate evolution, where accretion rates are measured at the inner disk boundary. Two scenarios of magnetic flux evolution are considered, namely, either total magnetic flux  $\Phi_B \propto M_d$ , or  $\Phi_B$  is constant. We see that at early stages, disk evolution proceeds very similarly in these two scenarios. After about 1 Myrs, the disk has lost about 30% of its mass through accretion and wind, and the subsequent evolutionary paths in the two scenarios diverge.

When assuming  $\Phi_B \propto M_d$ , the accretion rate gradually decreases with time as magnetic flux is lost, and the evolution slows down. Even after  $10^7$  years of evolution, the disk still possesses about 23% of its initial mass.

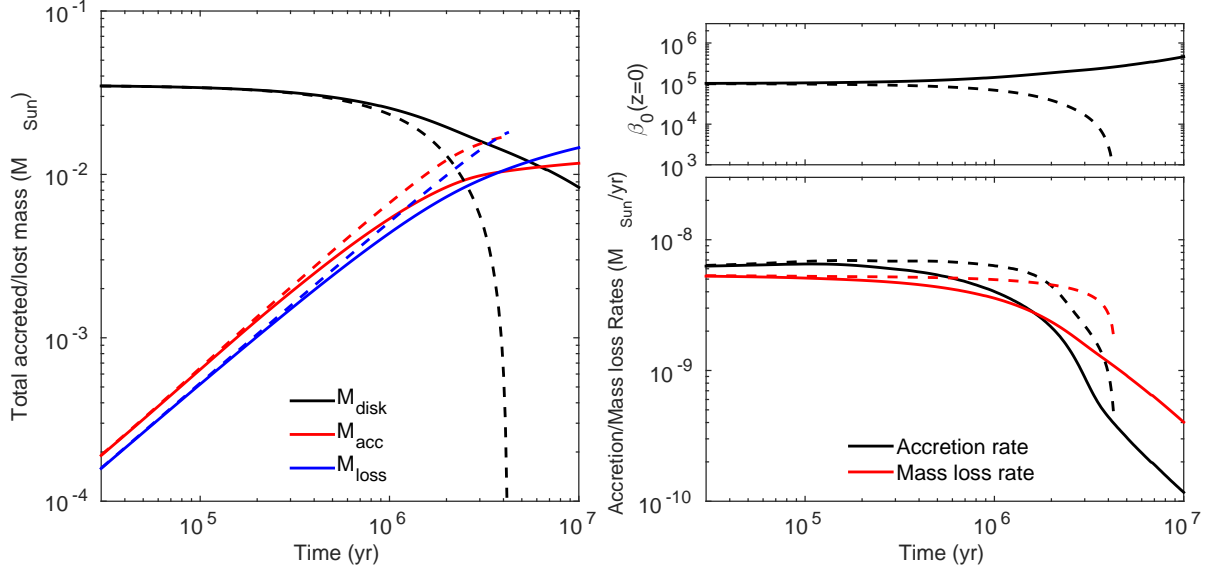


FIG. 6.— Left: Time evolution of total disk mass (black), mass accreted to the central protostar (red), and mass lost through the wind (blue). Right top: time evolution of midplane plasma  $\beta_0$ , assumed to be constant at all disk radii. Right bottom: time evolution of accretion rate at inner boundary (black) and total mass loss rate (red). In both panels, solid lines correspond to the case where total magnetic flux  $\Phi_B$  is set to be proportional to disk mass  $M_d$ , while dashed lines represent the case where  $\Phi_B$  is conserved.

We also see that midplane  $\beta_0$  slowly increases with time, and towards later evolution, wind mass loss rate exceeds accretion rate.

When assuming  $\Phi_B$  is constant, on the other hand, we see that accretion rate and mass loss rate maintain approximately a constant level for  $\sim 2$  Myrs. This is because magnetic field strength roughly stays constant in this scenario, which directly regulates accretion rates. Constant accretion/mass loss rates lead to rapid depletion of disk materials, and we see that total disk mass plunges down in a runaway manner shortly after  $t \sim 2$  Myrs. As the majority of disk mass is accreted or lost, FUV radiation can penetrate substantially deeper, enhancing the mass loss process relative to accretion. In the mean time, the MRI active zone grows and allows viscous spread to dominate in the outermost disk. The reduction of accretion rate near the end is a result of the redistribution of magnetic flux towards the outer disk (due to viscous spreading).

The two scenarios discussed here can be considered as two extreme limits on magnetic flux evolution. Rapid loss of magnetic flux leads to slow evolution and long disk lifetime, while conservation of magnetic flux leads to a two-timescale behavior: disk depletion occurs on timescales much shorter than disk lifetime. The latter behavior was also discussed by Armitage et al. (2013) when assuming constant total magnetic flux. The reality may lie in between the two extreme scenarios, which we use in the next subsection as a way to constrain disk lifetime.

For comparison, we also show in dash-dotted lines of Figure 5 results from a pure viscous disk evolution model assuming constant  $\alpha = 0.01$ . Besides the sequential drop in surface density, disk evolution is characterized by the expansion of the outer disk (viscous spreading). Over the course of a few Myrs, the disk size (defined by the radius above a certain threshold surface density) have expanded

by more than a factor of 2. This is much more significant than that in our fiducial disk evolution models, even viscous spreading dominates in the outermost region of the disk. Thus, we conclude that wind-dominated PPD evolution likely undergoes very little expansion of the outer disk as compared with viscous evolution models.

#### 4.2. Parameter Dependence

To better quantify the timescale of disk evolution and the significance of mass loss from disk winds, we have carried out a series of disk evolution calculations scanning the parameter space. Because we have found that the wind transport properties are the least sensitive to wind temperature  $T_a$ , we fix  $T_a/T_d = 3$  in all the calculations. We consider midplane plasma  $\beta_0 = 10^3, 10^4, 10^5$  and  $10^6$ , and FUV penetration depth  $\Sigma_{\text{FUV}} = 0.01$  and  $0.1 \text{ g cm}^{-2}$ .

We do not evolve the disk all the way to the end, but terminate the evolution when the disk has lost half of its mass, and call this time half disk lifetime  $t_{\text{half}}$ . We do so mainly because long-term evolution calculations likely bare large uncertainties due to our ignorance on magnetic flux evolution. For each set of parameters, we perform two runs, evolving the disk either assuming magnetic flux conservation  $\Phi_B = \text{const}$ , or  $\Phi_B \propto M_d$ . As discussed earlier, we may consider these two cases as two extreme scenarios, which set the lower and upper limits of  $t_{\text{half}}$ .<sup>6</sup> Similarly, we evaluate  $f_{\text{wind}}$ , the fractional mass loss from the wind compared to total mass loss due to both wind and accretion, over evolution time up to  $t_{\text{half}}$ .

In Figure 7, we plot  $t_{\text{half}}$  and  $f_{\text{wind}}$  from all runs in this parameter study, organized as a function of initial mid-

<sup>6</sup> Observationally, disk lifetime is inferred statistically by counting disk fraction (Haisch et al. 2001), which reflects full disk lifetime  $t_{\text{full}}$ . Based on our results, if magnetic flux is approximately conserved during disk evolution, we approximately have  $t_{\text{half}} \sim t_{\text{full}}/2$ . If the disk loses magnetic flux, then  $t_{\text{half}} < t_{\text{full}}/2$ .



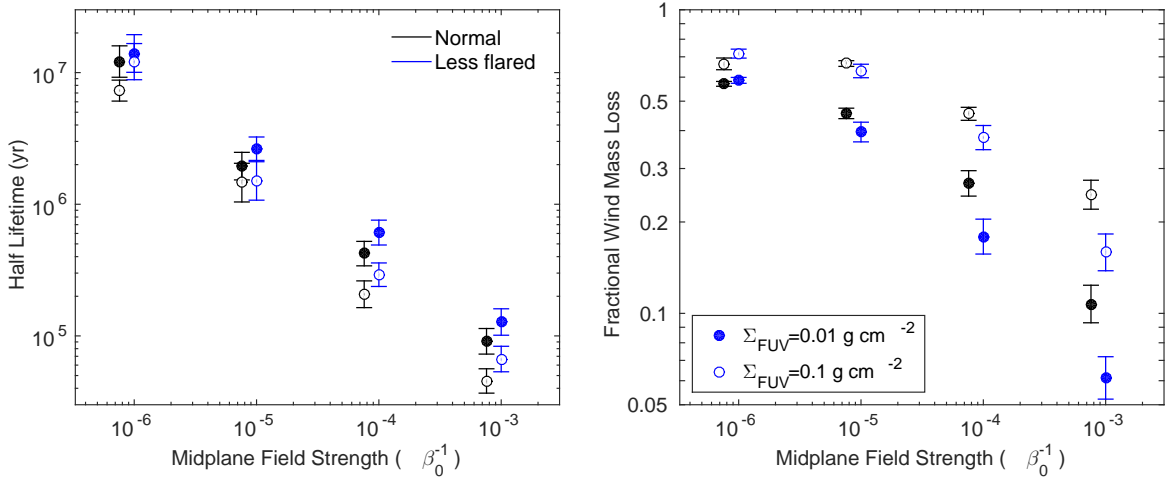


FIG. 7.— Half disk lifetime ( $t_{\text{half}}$  left) and fractional mass loss via disk wind ( $f_{\text{wind}}$ , right) from all our global disk evolution calculations. Each symbol reflects two disk evolution calculations, assuming total magnetic flux  $\Phi_B \propto M_d$  (disk mass) or  $\Phi_B = \text{const}$ . They are marked as upper and lower limits, with their geometric mean marked by the circle. Filled and open circles correspond to calculations assuming  $\Sigma_{\text{FUV}} = 0.01 \text{ g cm}^{-2}$  and  $0.1 \text{ g cm}^{-2}$ , respectively. Black and blue symbols correspond normal flared disks with  $s_T = 0.5$  and less flared disks with  $s_T = 0.7$  (see Equation 10). Symbols are organized as a function of midplane field strength (characterized by  $\beta_0$ ), and at the same  $\beta_0$ , symbols with different colors are slightly offset from one another for better visualization.

plane  $\beta_0$ . It best summarizes the main results discussed in this paper.

Disk lifetime is determined by a combination of mass accretion and mass loss processes. It mostly depends on the amount of magnetic flux threading the disks. For our fiducial disk model, midplane plasma  $\beta_0 \sim 10^5$  yields  $2 \times t_{\text{half}}$  that is in best agreement with observational constraints of disk lifetime (e.g., Haisch et al. 2001; Fedele et al. 2010) on a few Myr time scale. It also supports the interpretation of fossil magnetic field measurement of the solar nebular (Fu et al. 2014). Note that increasing or reducing the field strength by a factor of only  $\sim 3$  (a factor  $\sim 10$  change in  $\beta_0$ ) would yield disk lifetime that is either too short or too long.

All calculations with  $\beta_0 = 10^5$  yield a fractional wind mass loss  $f_{\text{wind}}$  around one half (0.3–0.7). Wind mass loss becomes progressively less important towards stronger disk magnetization, but such scenario is very unlikely as constrained by disk lifetime. Therefore, we expect that wind mass loss plays a rather significant role in global disk evolution.

Enhanced FUV luminosity (hence its penetration) leads to both enhanced accretion rate, and to a higher level, outflow rates (and hence larger  $f_{\text{wind}}$ ). In our fiducial model,  $f_{\text{wind}}$  increases from 0.45 to 0.65 as  $\Sigma_{\text{FUV}}$  increases from 0.01 to  $0.1 \text{ g cm}^{-2}$ , which manifests what we termed magneto-photoevaporation in B16. The contrast between mass accretion and outflow is more prominent as the disk becomes more strongly magnetized. On the other hand, because of the relatively gentle dependence of  $\dot{M}_{\text{acc}}$  and  $\dot{M}_{\text{wind}}$  on  $\Sigma_{\text{FUV}}$  (see Figure 4), reduction of  $t_{\text{half}}$  is only modest. A factor of 10 difference in  $\Sigma_{\text{FUV}}$  typically leads to a factor of at most 3 difference in  $t_{\text{half}}$ .

## 5. MODEL EXTENSION

### 5.1. Level of Disk Flaring

In this subsection, we consider disks that are less flared, which is expected to affect the penetration of

FUV/X-rays in heating/ionizing the disk surface layer. Although the temperature structure of PPDs is not well constrained observationally, this study is in part motivated by the SED-based classification of Herbig Ae/Be disks that show two distinct groups with either flared or flat geometry (Meeus et al. 2001). It has recently been found that flared Herbig Ae/Be disks all have large gaps (Maaskant et al. 2013), and some flat disks may have small gaps (Menu et al. 2015), suggesting an evolutionary path starting from flat full disks towards flared transition disks. Note that this classification mainly reflects disk geometry at  $\sim \text{AU}$  scale, where flat disks are generally attributed to self-shadowing by puffed inner rims (Dullemond & Dominik 2004). Even many disks are considered “flat”, they can become flared towards larger radii (e.g., Rosenfeld et al. 2013 for the HD 163296 disk). Despite the complications and uncertainties in our understandings of disk geometry and temperature structure, we aim to assess whether they can significantly affect disk wind/transport properties in a qualitative manner by simply varying the parameter  $s_T$ . Note that  $s_T = 1$  would lead to a constant  $H/R$ , which is unlikely to be realized on a global scale when balancing passive stellar heating with thermal radiation.

In Figure 8, we compare the results from our fiducial model with normal level of flaring (fiducial,  $s_T = 0.5$ ), a model with less flaring ( $s_T = 0.7$ ), and an almost flat disk ( $s_T = 0.9$ ). Note that increasing  $s_T$  makes the disk cooler towards the outer disk, with smaller disk scale height  $H_d$ . Correspondingly, the geometric location of the FUV front  $z_a$  becomes lower. On the other hand, we see from the left panel of the Figure that when normalized to disk scale height,  $z_a/H_d$  becomes progressively higher as the disk becomes less flared. This is simply a geometric effect that at the same  $z/H_d$ , sight lines to the central star would encounter larger column density of gas in a less flared disk. In addition, we see that in less flared disks, the size of the MRI active zone shrinks. This is also natural consequence of larger  $z_a/H_d$ . With  $s_T = 0.7$ , the inner edge of the MRI active zone is already at  $R > R_d$  in our

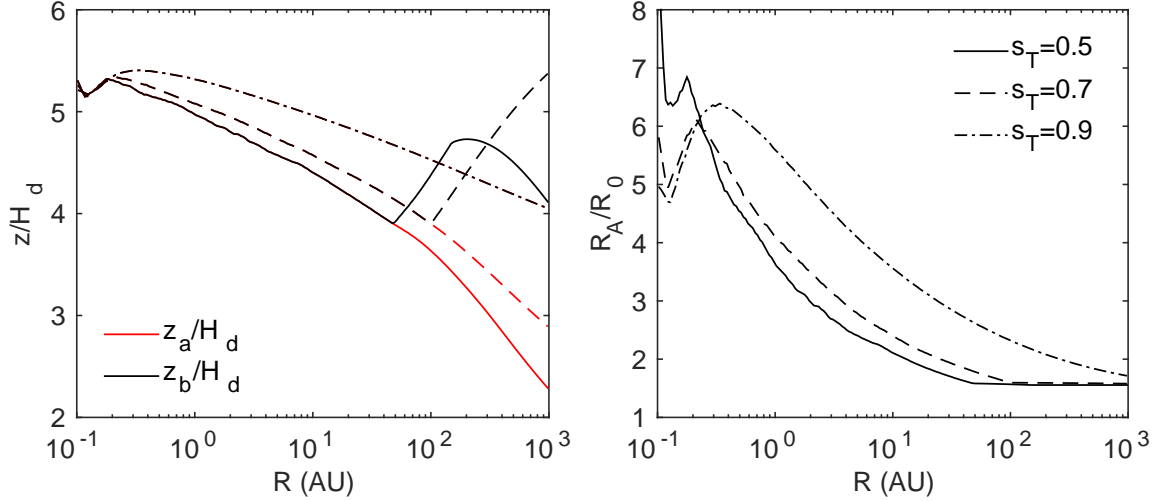


FIG. 8.— Representative calculation results using different disk flaring parameter  $s_T$  (power law index of radial temperature gradient), with  $s_T = 0.5$  (solid, normal flaring),  $s_T = 0.7$  (dashed, less flared) and  $s_T = 0.9$  (dash-dotted, almost flat). Left: radial profiles for locations of the FUV front  $z_a$  (red) and the wind base  $z_b$  (black), normalized to disk scale height  $H_d$ . Right: radial profiles for the ratio of Alfvén radius to wind launching radius  $R_A/R_0$ . All other parameters are fiducial ( $\beta_0 = 10^5$ ,  $\Sigma_{\text{FUV}} = 0.01 \text{ g cm}^{-2}$ ,  $T_a/T_d = 3$ ).

disk model, while for a nearly flat disk with  $s_T = 0.9$ , the MRI active zone diminishes: the entire disk becomes largely laminar.

With larger  $z_a/H_d$  in less flared disks, the wind base density and pressure is smaller, making the wind base region effectively more strongly magnetized. As shown in the right panel of Figure 8, the Alfvén radius becomes larger in less flared disks. This means that wind mass loss rate becomes a smaller fraction of accretion rate (see Equation (25)). This is also reflected in Figure 7, where we also show results of  $t_{\text{half}}$  and fraction mass loss with  $s_T = 0.7$ . Overall, the situation for less flared disk is similar to the case with smaller  $\Sigma_{\text{FUV}}$ : less flared disks lead to a reduction of both wind-driven accretion rate and mass loss rate (and hence longer  $t_{\text{half}}$ ), but the reduction of mass loss rate is more significant.

### 5.2. Effect of X-ray Heating

The studies in the preceding sections have implicitly assumed that X-rays and FUV have similar penetration depth, as described in Section 2.2. In reality, FUV penetration depth is very uncertain depending on the abundance of very small grains, while absorption of X-ray photons is insensitive to grain abundance, and depends mainly on photon energy (Igea & Glassgold 1999; Ercolano & Glassgold 2013). For typical photon energy of 1 keV, the X-ray penetration depth is on the order  $10^{22} \text{ cm}^{-2}$  (e.g., Owen et al. 2010), and it becomes larger for higher photon energies. This is at least comparable to the fiducial value of  $\Sigma_{\text{FUV}} = 0.01 \text{ g cm}^{-2}$  that we have adopted. However, considering the full X-ray spectrum with the presence of harder X-rays, the overall penetration depth is likely higher. In this subsection, we relax our previous assumption and allow X-rays to penetrate deeper than the FUV. We define X-ray penetration depth  $\Sigma_X \geq \Sigma_{\text{FUV}}$ , which determines the location of atmosphere  $z_a$ . Gas temperature is set to  $T = T_d$  for  $z < z_a$  and  $T = T_a$  for  $z > z_a$ , as before.<sup>7</sup> Let  $z_f$  be the height

of the FUV ionization front set by  $\Sigma_{\text{FUV}}$ , and  $z_f \geq z_a$ . The wind base is assumed to be located at  $z_b = z_f$  if gas is sufficiently magnetized to suppress the MRI, otherwise,  $z_b$  is set to larger values according to the prescription in Section 2.2.4.

In Figure 9, we compare the results from our fiducial model with  $\Sigma_{\text{FUV}} = \Sigma_X = 0.01 \text{ g cm}^{-2}$  (solid lines) with a calculation assuming  $\Sigma_X = 0.1 \text{ g cm}^{-2}$  (dashed lines). The left panel shows the value of Alfvén radius normalized to wind launching radius. We see that despite that X-rays can heat into deeper regions in the disk, leading to substantial differences in disk vertical density and temperature structures, the wind properties resulting from the two cases are remarkably similar. This is most easily understood from the example in the right panel, where we show the vertical pressure profiles at 1 AU in the two cases. With  $T = T_a$  at disk surface layer, the density profile, as well as pressure profile, are in the form of  $e^{-z^2/H_a^2}$ . If we assume the column densities (from a position at disk surface) radially towards the star and vertically towards large  $z$  are proportional to each other (which approximately holds for flared disks where column density is dominated by local contributions), then for a given  $\Sigma_{\text{FUV}}$ , the density and pressure at the FUV ionization front  $z_f$  ( $= z_b$  in this case) are largely unchanged regardless of whether X-rays penetrate deeper or not. In this example, we find the pressure (and density) difference between the two cases at  $z = z_f$  is only 15%, which explains the very small difference in  $R_A$ . Therefore, we conclude that density and pressure at the wind base (and hence the main wind properties) is largely insensitive to additional heating by X-rays below the FUV ionization front. We have also verified this result using higher atmosphere temperature  $T_a = 8T_d$ , and with larger  $\Sigma_X$  up to  $0.5 \text{ g cm}^{-2}$ .

profile with a sharp temperature transition at  $z = z_a$  may no longer be a good approximation. However, we mainly aim at a proof-of-concept study on the role of deeper X-ray heating, and a two-temperature treatment should suffice for this purpose.

<sup>7</sup> We note that in reality, X-ray heating profile is likely much more smooth than the FUV case, and hence the two-temperature

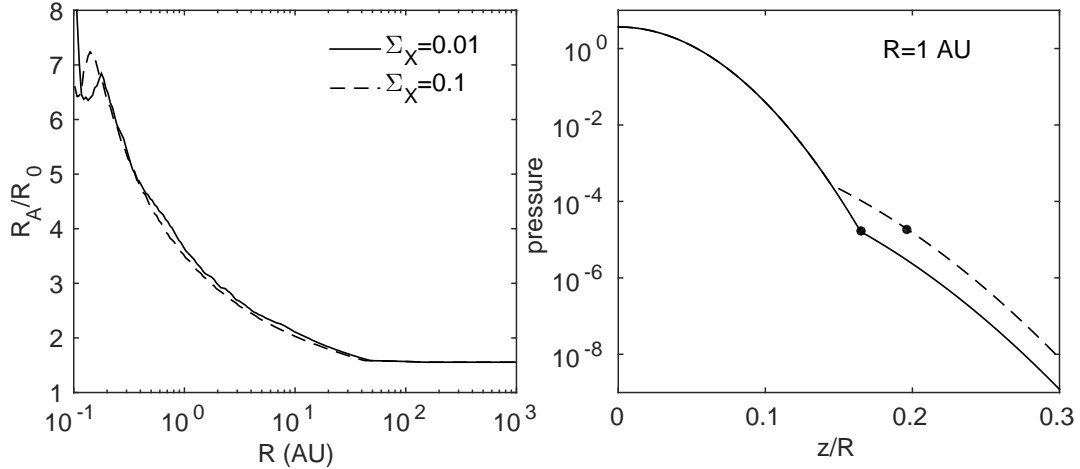


FIG. 9.— Calculation results using different X-ray penetration depth  $\Sigma_X$ , with  $\Sigma_X = 0.01 \text{ g cm}^{-2} = \Sigma_{\text{FUV}}$  (solid) and  $\Sigma_X = 0.1 \text{ g cm}^{-1}$  (dashed). Left: radial profiles for the ratio of Alfvén radius to wind launching radius  $R_A/R_0$ . Right: vertical pressure profile at 1 AU. The black dots mark the FUV ionization front given by  $\Sigma_{\text{FUV}} = 0.01 \text{ g cm}^{-1}$ . All other parameters are fiducial ( $\beta_0 = 10^5$ ,  $\Sigma_{\text{FUV}} = 0.01 \text{ g cm}^{-2}$ ,  $T_a/T_d = 3$ ). See section 5.2 for details.

## 6. DISCUSSION

### 6.1. Relation to Photoevaporation

Photoevaporation has long been considered as the primary mechanism for the dispersal of PPDs. As a pure thermal wind, it does not exert a torque to the disk, and hence would evaporate the disk regardless of internal processes of disk angular momentum transport. However, as MHD wind has been realized to play the dominant role in disk angular momentum transport, we expect real PPD winds to be magnetized in nature, and they are externally heated. Therefore, wind mass loss and angular momentum transport are intrinsically coupled. They are both affected by thermal effects, and they jointly determine global disk evolution.

Incorporating the magneto-thermal disk wind model of B16, our model has included, in a simple approximate manner, all major ingredients of the aforementioned new framework of global disk evolution. Compared with photoevaporation calculations, wind mass loss in our calculations is directly coupled to angular momentum transport, instead of being treated separately. This leads to the correlation between disk lifetime and fractional wind mass loss, as a natural consequence of MHD disk wind.

Photoevaporation calculations are highly sensitive to the treatment of thermodynamics, which leads to considerable discrepancies between different models such as those driven by Extreme UV (e.g., Hollenbach et al. 1994; Alexander et al. 2006), X-rays (e.g., Ercolano et al. 2009; Owen et al. 2010), and FUV (e.g., Adams et al. 2004; Gorti et al. 2009). While our calculations have treated thermodynamics in a highly simplified manner, our main results suggest that wind mass loss is only modestly sensitive to thermodynamic effects, whereas the dominant role is played by amount of magnetic flux. As suggested in B16, a unified description of disk wind mass loss would be better termed “magneto-photoevaporation”.

Photoevaporation has been commonly invoked as an explanation of (a fraction of) transition disks, a small fraction of PPDs characterized by the presence of large inner gaps/holes, by inside-out clearing (see Owen 2015

for a review). In the MHD framework, whether the disk can be cleared inside-out depends on the details of magnetic flux evolution, which remains poorly understood. For instance, if the inner disk is capable of maintaining its total magnetic flux (e.g., possibly due to the Hall effect), while the outer disk loses flux (i.e., as a result of ambipolar diffusion), then inside-out clearing would be a natural consequence.

### 6.2. Implications

One important implication of wind mass loss is that mass is primarily removed from disk surface, while in low turbulent environment, most dust/solids settle and reside around disk midplane. The removal of largely dust-free gas, and in combination with radial drift (e.g., Youdin & Shu 2002), can directly enhance the dust-to-gas mass ratio, creating favorable conditions for planetesimal formation (Johansen et al. 2009b), and particularly allowing for smaller, more strongly coupled dust to participate in planetesimal formation (Bai & Stone 2010; Carrera et al. 2015). Dust evolution has been incorporated in the recent study by Gorti et al. (2015) in the context of photoevaporation on top of viscous disk evolution, and they found significant enhancement of dust-to-gas ratio as a robust outcome of surface mass loss. We thus expect the same conclusion to hold in the MHD wind, or magneto-photoevaporation framework. The fact that wind mass loss is most significant towards the outer disk implies that the enhancement of dust-to-gas ratio may proceed from the outer disk inward.

Signatures of wind from PPDs have been routinely observed in the form of blue-shifted emission lines such as from CO, OI and NeII lines (e.g., Pascucci & Sterzik 2009; Pontoppidan et al. 2011; Herczeg et al. 2011), but constraining the wind mass loss rate from line data is extremely difficult.<sup>8</sup> Natta et al. (2014) recently reported  $\dot{M}_{\text{loss}}/\dot{M}_{\text{acc}}$  in the range of 0.1 – 1 with large uncertainties. With typical blueshift of the order a few  $\text{km s}^{-1}$  and

<sup>8</sup> For the high-velocity jet,  $\dot{M}_{\text{loss,jet}}/\dot{M}_{\text{acc}}$  is found to be of the order 0.1 with large uncertainties (Hartigan et al. 1995).



given the excitation conditions, the wind most likely originates from the inner few AU. Our results suggest that the inferred mass loss rate only represents a small fraction ( $< 20 - 30\%$ ) of total disk wind mass loss. Within the uncertainties, the measurements are consistent with our expectations of  $\dot{M}_{\text{loss}} \gtrsim \dot{M}_{\text{acc}}$ .

We have discussed in Section 3.1.3 that the column density in the wind flow can provide shielding for the UV radiation from the protostar. Wind shielding has also been discussed in the context of survival of molecules (Panoglou et al. 2012). In reality, FUV penetration is largely determined by the abundance of very small grains in the disk surface and wind column, which is very poorly known. We speculate that if very small grains are sufficiently abundant at disk surface, they can be efficiently lifted by the wind (e.g., Miyake et al. 2016), which can substantially enhance the FUV opacity. The non-detection of turbulent motion towards the outer region of Herbig Ae disk HD 163296 (Flaherty et al. 2015) also indirectly suggests that shielding of FUV radiation may reduce or even quench the MRI zone in the outer disk. Our fiducial choice of a relatively small  $\Sigma_{\text{FUV}}$  reflects such considerations, but the potentially important effect of wind shielding calls for further study.

### 6.3. Limitations and Future Directions

Our global model inherits from the wind model of B16, thus share the same uncertainties, especially from the fact that we prescribe the wind geometry instead of solving cross-field force balance. However, as discussed there, more uncertainties arise from our ignorance about magnetic flux distribution, which eventually determines the wind geometry. Thus, B16 chose to parameterize the disk geometry and focus on wind physics along prescribed field lines. Our global wind model follows the same logic, and mainly explores the consequence of the B16 model at a global scale.

Our wind model may suffer from two systematic uncertainties. The first arises from a potentially systematic variation of wind geometry with radius. For instance, global wind simulations (e.g., Zanni et al. 2007; Stepanovs & Fendt 2014) typically find that towards larger radii, the wind inclination angle  $\theta$  increases, and wind field lines get more divergent. We have adopted fixed wind geometry parameters  $\theta = 45^\circ$  and  $q = 0.25$  in this work. Based on results from the B16 model, with field lines getting more inclined and more divergent, the Alfvén radius (lever arm) would decrease, leading to more pronounced fractional mass loss towards the outer disk. The second uncertainty arises from the extension of the B16 wind model to wind launched from the MRI active region, whereas the model is intended for a laminar wind. Wind launching in the MRI case is a robust phenomenon as observed in local simulations (Suzuki & Inutsuka 2009; Bai & Stone 2013a; Fromang et al. 2013; Simon et al. 2013a), and the field configuration is fully dominated by the toroidal component indicating wind launching by magnetic pressure gradient, similar to the laminar wind in PPDs discussed in B16. We thus expect our treatment at least qualitatively reflects the relation between mass loss and angular momentum transport in this regime, while global simulations are certainly needed to better calibrate wind

kinematics.

Our calculations parameterize the role of thermodynamics simply in terms of FUV (and X-ray) penetration, constant wind temperature and level of disk flaring. In reality, radiative transfer and photo-chemistry are essential to better quantify thermodynamical effects. Due to the important role played by grain opacity, these are coupled with the size distribution and spatial distribution of dust grains, which in turn are coupled to disk dynamics. The interplay among dynamics, dust evolution, chemistry, and radiation in the system may result in much richer phenomenology than considered here, and are worth more in-depth investigations.

The sensitive dependence of wind and transport properties on magnetic field strength calls for better understandings of magnetic flux transport, as already discussed in Section 2.2.3. Moreover, the starting point of our evolution calculations is motivated from a typical disk at Class II phase. Disk evolution starts from much earlier phases, and magnetic flux is well known to control disk dynamics from the disk formation stage (see Li et al. 2014 for a review). In particular, the Hall effect could induce a bimodality on initial disk size depending on the polarity of the background magnetic field with respect to disk rotation axis (Tsukamoto et al. 2015; Wurster et al. 2016), and such bimodality is likely to be carried into all later phases of disk evolution (Wardle & Salmeron 2012; Bai 2014, 2015; Simon et al. 2015). How the Hall effect affect magnetic flux evolution is unknown, but hints for strong polarity dependence exist from local studies (Bai 2014). Our Figure 7 shows that to reproduce observed PPD lifetime, the amount of magnetic flux is constrained to a relatively narrow range. Some feedback and self-regulation mechanism might be involved in magnetic flux evolution. Future global simulations of wind-driven disk evolution with resolved disk microphysics are essential to address these problems.

## 7. SUMMARY AND CONCLUSIONS

In this work, we have constructed a framework to study global evolution of PPDs that incorporates wind-driven accretion, wind mass loss, and viscous transport. The magneto-thermal wind model the B16 is adopted as the primary ingredient of the framework. The model is motivated by recent local simulations of PPD gas dynamics that have properly incorporated disk microphysics, which suggest that the MRI is largely suppressed in the disk interior and magnetized wind is launched in the externally heated and ionized surface layer from the FUV ionization front (Bai & Stone 2013b; Gressel et al. 2015). We further consider the fact that the well ionized surface layer can be subject to the MRI in the outer region of PPDs (Perez-Becker & Chiang 2011; Simon et al. 2013a), depending on the strength of vertical magnetic field fields and FUV penetration depth, which contributes to viscous angular momentum transport. Ideally, disk evolution should be coupled with a procedure for magnetic flux evolution. The latter is treated phenomenologically in this work by assuming constant midplane plasma  $\beta_0$ , but can be improved upon better understanding of magnetic flux transport in PPDs.

Our main findings include

- Disk evolution is largely dominated by MHD wind-

driven accretion and mass loss. Contribution from the MRI can be important in the outermost disk but viscous spread is suppressed.

- The disk evolution timescale sensitively depends on the amount of magnetic flux threading PPDs. Disk dispersal is rapid if the disk is able to retain most of its magnetic flux during evolution, otherwise, disk dispersal is gradual.
- Given typical disk lifetime of a few Myrs, the disk loses comparable amount of mass via disk wind and accretion. Most of the wind mass loss proceeds through the outer disk ( $\gtrsim 10$  AU). Fractional mass loss via disk wind increases with decreasing disk magnetization (increasing disk lifetime).
- The depth of FUV penetration and level of disk flaring are the main thermodynamic factors affecting disk evolution. Smaller FUV penetration depth and less flared geometry slightly reduce wind-driven accretion rate, and more strongly reduces fractional wind mass loss.

In addition, the column density in the wind flow can provide a modest level of shielding to stellar UV radiation, especially if the wind lifts very small dust grains.

This work represents an initial effort towards modeling global evolution of PPDs that incorporates realistic disk physics. At the moment, we have mainly focused on the evolution of the overall mass budget, and significant wind mass loss likely substantially enhances the disk dust-to-gas mass ratio and directly promotes planetesimal formation. Better knowledge on magnetic flux evolution is needed to make reliable predictions on the details of disk surface density evolution, allowing for more realistic studies of planet formation.

I thank Kees Dullemond and Antonella Natta for encouraging me to work on this project, and Sean Andrews for useful discussions. I also thank Jeremy Goodman, Antonella Natta, Kees Dullemond, and an anonymous referee for carefully reading of the manuscript and providing useful feedback that improves this paper. This work is supported by Institute for Theory and Computation at Harvard University.

## APPENDIX

## REFERENCES

- Adams, F. C., Hollenbach, D., Laughlin, G., & Gorti, U. 2004, *ApJ*, 611, 360
- Alexander, R., Pascucci, I., Andrews, S., Armitage, P., & Cieza, L. 2014, *Protostars and Planets VI*, 475
- Alexander, R. D., Clarke, C. J., & Pringle, J. E. 2006, *MNRAS*, 369, 216
- ALMA Partnership. 2015, *ApJ*, 808, L3
- Andrews, S. M., Wilner, D. J., Hughes, A. M., Qi, C., & Dullemond, C. P. 2009, *ApJ*, 700, 1502
- . 2010, *ApJ*, 723, 1241
- Armitage, P. J. 2011, *ARA&A*, 49, 195
- Armitage, P. J., Simon, J. B., & Martin, R. G. 2013, *ApJ*, 778, L14
- Bai, X.-N. 2011, *ApJ*, 739, 50
- . 2013, *ApJ*, 772, 96
- . 2014, *ApJ*, 791, 137
- . 2015, *ApJ*, 798, 84
- Bai, X.-N. & Goodman, J. 2009, *ApJ*, 701, 737
- Bai, X.-N. & Stone, J. M. 2010, *ApJ*, 722, L220
- . 2013a, *ApJ*, 767, 30
- . 2013b, *ApJ*, 769, 76
- . 2014, *ApJ*, 796, 31
- Bai, X.-N., Ye, J., Goodman, J., & Yuan, F. 2016, *ApJ*, 818, 152
- Balbus, S. A. & Hawley, J. F. 1991, *ApJ*, 376, 214
- Bans, A. & Königl, A. 2012, *ApJ*, 758, 100
- Baruteau, C., Crida, A., Paardekooper, S.-J., Masset, F., Guilet, J., Bitsch, B., Nelson, R., Kley, W., & Papaloizou, J. 2014, *Protostars and Planets VI*, 667
- Bethell, T. J. & Bergin, E. A. 2011, *ApJ*, 739, 78
- Carrera, D., Johansen, A., & Davies, M. B. 2015, *A&A*, 579, A43
- Chiang, E. I. & Goldreich, P. 1997, *ApJ*, 490, 368
- Combet, C. & Ferreira, J. 2008, *A&A*, 479, 481
- Desch, S. J. & Turner, N. J. 2015, *ApJ*, 811, 156
- Dullemond, C. P. & Dominik, C. 2004, *A&A*, 417, 159
- Ercolano, B., Clarke, C. J., & Drake, J. J. 2009, *ApJ*, 699, 1639
- Ercolano, B. & Glassgold, A. E. 2013, *MNRAS*, 436, 3446
- Faure, J., Fromang, S., & Latter, H. 2014, *A&A*, 564, A22
- Fedele, D., van den Ancker, M. E., Henning, T., Jayawardhana, R., & Oliveira, J. M. 2010, *A&A*, 510, A72
- Ferreira, J. & Pelletier, G. 1995, *A&A*, 295, 807
- Flaherty, K. M., Hughes, A. M., Rosenfeld, K. A., Andrews, S. M., Chiang, E., Simon, J. B., Kerzner, S., & Wilner, D. J. 2015, *ApJ*, 813, 99
- Fromang, S., Latter, H., Lesur, G., & Ogilvie, G. I. 2013, *A&A*, 552, A71
- Fu, R. R., Weiss, B. P., Lima, E. A., Harrison, R. J., Bai, X.-N., Desch, S. J., Ebel, D. S., Suavet, C., Wang, H., Glenn, D., Le Sage, D., Kasama, T., Walsworth, R. L., & Kuan, A. T. 2014, *Science*, 346, 1089
- Gorti, U., Dullemond, C. P., & Hollenbach, D. 2009, *ApJ*, 705, 1237
- Gorti, U., Hollenbach, D., & Dullemond, C. P. 2015, *ApJ*, 804, 29
- Gressel, O. & Pessah, M. E. 2015, *ApJ*, 810, 59
- Gressel, O., Turner, N. J., Nelson, R. P., & McNally, C. P. 2015, *ApJ*, 801, 84
- Guilet, J. & Ogilvie, G. I. 2012, *MNRAS*, 424, 2097
- . 2014, *MNRAS*, 441, 852
- Haisch, Jr., K. E., Lada, E. A., & Lada, C. J. 2001, *ApJ*, 553, L153
- Hartigan, P., Edwards, S., & Ghandour, L. 1995, *ApJ*, 452, 736
- Hawley, J. F., Gammie, C. F., & Balbus, S. A. 1995, *ApJ*, 440, 742
- Hayashi, C. 1981, *Progress of Theoretical Physics Supplement*, 70, 35
- Henning, T. & Semenov, D. 2013, *Chemical Reviews*, 113, 9016
- Herczeg, G. J., Brown, J. M., van Dishoeck, E. F., & Pontoppidan, K. M. 2011, *A&A*, 533, A112
- Herczeg, G. J., Wood, B. E., Linsky, J. L., Valenti, J. A., & Johns-Krull, C. M. 2004, *ApJ*, 607, 369
- Hirose, S. 2015, *MNRAS*, 448, 3105
- Hollenbach, D., Johnstone, D., Lizano, S., & Shu, F. 1994, *ApJ*, 428, 654
- Igea, J. & Glassgold, A. E. 1999, *ApJ*, 518, 848
- Johansen, A., Youdin, A., & Klahr, H. 2009a, *ApJ*, 697, 1269
- Johansen, A., Youdin, A., & Mac Low, M. 2009b, *ApJ*, 704, L75
- Klahr, H. & Hubbard, A. 2014, *ApJ*, 788, 21
- Lesur, G., Kunz, M. W., & Fromang, S. 2014, *A&A*, 566, A56
- Li, Z.-Y., Banerjee, R., Pudritz, R. E., Jørgensen, J. K., Shang, H., Krasnopolsky, R., & Maury, A. 2014, *Protostars and Planets VI*, 173
- Lubow, S. H., Papaloizou, J. C. B., & Pringle, J. E. 1994, *MNRAS*, 267, 235
- Lyra, W. 2014, *ApJ*, 789, 77
- Maaskant, K. M., Honda, M., Waters, L. B. F. M., Tielens, A. G. G. M., Dominik, C., Min, M., Verhoeff, A., Meeus, G., & van den Ancker, M. E. 2013, *A&A*, 555, A64

- Marcus, P., Pei, S., Jiang, C.-H., Barranco, J., Hassanzadeh, P., & Lecoanet, D. 2014, *ApJ*, submitted
- Meeus, G., Waters, L. B. F. M., Bouwman, J., van den Ancker, M. E., Waelkens, C., & Malfait, K. 2001, *A&A*, 365, 476
- Menu, J., van Boekel, R., Henning, T., Leinert, C., Waelkens, C., & Waters, L. B. F. M. 2015, *A&A*, 581, A107
- Miyake, T., Suzuki, T. K., & Inutsuka, S.-i. 2016, *ApJ*, submitted
- Natta, A., Testi, L., Alcalá, J. M., Rigliaco, E., Covino, E., Stelzer, B., & D'Elia, V. 2014, *A&A*, 569, A5
- Nelson, R. P., Gressel, O., & Umurhan, O. M. 2013, *MNRAS*, 435, 2610
- Okuzumi, S. & Hirose, S. 2011, *ApJ*, 742, 65
- Okuzumi, S., Takeuchi, T., & Muto, T. 2014, *ApJ*, 785, 127
- Owen, J. E. 2015, *ArXiv e-prints*
- Owen, J. E., Ercolano, B., Clarke, C. J., & Alexander, R. D. 2010, *MNRAS*, 401, 1415
- Panoglou, D., Cabrit, S., Pineau Des Forêts, G., Garcia, P. J. V., Ferreira, J., & Casse, F. 2012, *A&A*, 538, A2
- Pascucci, I. & Sterzik, M. 2009, *ApJ*, 702, 724
- Perez-Becker, D. & Chiang, E. 2011, *ApJ*, 735, 8
- Pontoppidan, K. M., Blake, G. A., & Smette, A. 2011, *ApJ*, 733, 84
- Raettig, N., Lyra, W., & Klahr, H. 2013, *ApJ*, 765, 115
- Rosenfeld, K. A., Andrews, S. M., Hughes, A. M., Wilner, D. J., & Qi, C. 2013, *ApJ*, 774, 16
- Shakura, N. I. & Sunyaev, R. A. 1973, *A&A*, 24, 337
- Simon, J. B., Bai, X.-N., Armitage, P. J., Stone, J. M., & Beckwith, K. 2013a, *ApJ*, 775, 73
- Simon, J. B., Bai, X.-N., Stone, J. M., Armitage, P. J., & Beckwith, K. 2013b, *ApJ*, 764, 66
- Simon, J. B., Lesur, G., Kunz, M. W., & Armitage, P. J. 2015, *MNRAS*, 454, 1117
- Sorathia, K. A., Reynolds, C. S., & Armitage, P. J. 2010, *ApJ*, 712, 1241
- Steinacker, A. & Papaloizou, J. C. B. 2002, *ApJ*, 571, 413
- Stepanovs, D. & Fendt, C. 2014, *ApJ*, 793, 31
- Stoll, M. H. R. & Kley, W. 2014, *A&A*, 572, A77
- Suzuki, T. K. & Inutsuka, S.-i. 2009, *ApJ*, 691, L49
- . 2014, *ApJ*, 784, 121
- Takeuchi, T. & Okuzumi, S. 2014, *ApJ*, 797, 132
- Testi, L., Birnstiel, T., Ricci, L., Andrews, S., Blum, J., Carpenter, J., Dominik, C., Isella, A., Natta, A., Williams, J. P., & Wilner, D. J. 2014, *Protostars and Planets VI*, 339
- Tsukamoto, Y., Iwasaki, K., Okuzumi, S., Machida, M. N., & Inutsuka, S. 2015, *ApJ*, 810, L26
- Turner, N. J., Fromang, S., Gammie, C., Klahr, H., Lesur, G., Wardle, M., & Bai, X.-N. 2014, *Protostars and Planets VI*, 411
- Walsh, C., Millar, T. J., & Nomura, H. 2010, *ApJ*, 722, 1607
- Wardle, M. 2007, *Ap&SS*, 311, 35
- Wardle, M. & Koenigl, A. 1993, *ApJ*, 410, 218
- Wardle, M. & Salmeron, R. 2012, *MNRAS*, 422, 2737
- Weber, E. J. & Davis, Jr., L. 1967, *ApJ*, 148, 217
- Weidenschilling, S. J. 1977, *Ap&SS*, 51, 153
- Wurster, J., Price, D. J., & Bate, M. R. 2016, *MNRAS*, 457, 1037
- Xu, R. & Bai, X.-N. 2016, *ApJ*, in press
- Youdin, A. N. & Shu, F. H. 2002, *ApJ*, 580, 494
- Zanni, C., Ferrari, A., Rosner, R., Bodo, G., & Massaglia, S. 2007, *A&A*, 469, 811